Title

A NUMERICAL STUDY OF OBLIQUE-SHOCK WAVE REFLECTIONS WITH EXPERIMENTAL COMPARISONS

Author

Glaz, H.M.

Publication Date

1984-08-01

UC-34

LBL-18156
Preprint c.1

Lawrence Berkeley Laboratory
UNIVERSITY OF CALIFORNIA

Physics Division

Mathematics Department

To be submitted for publication

A NUMERICAL STUDY OF OBLIQUE-SHOCK WAVE REFLECTIONS WITH EXPERIMENTAL COMPARISONS

H.M. Glaz, P. Colella, I.I. Glass,
and R.L. Deschambault

August 1984

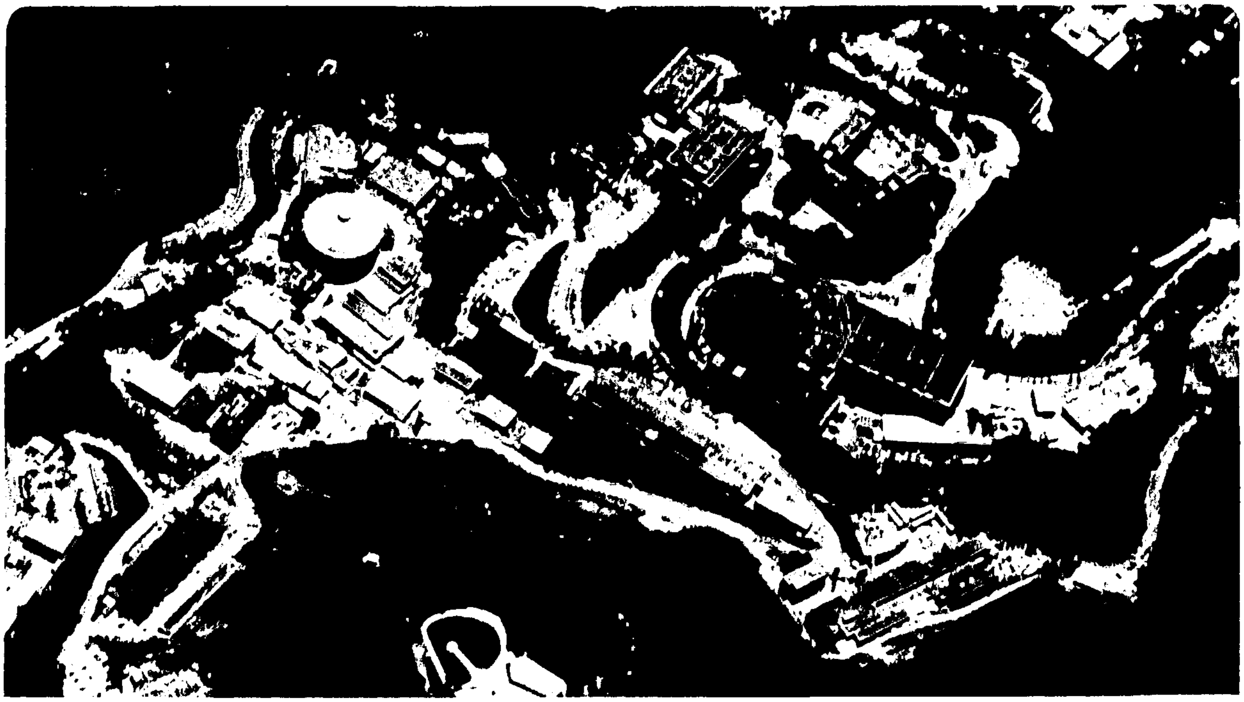

Prepared for the U.S. Department of Energy under Contract DE-AC03-76SF00098

LBL-18156

A NUMERICAL STUDY OF OBLIQUE-SHOCK WAVE REFLECTIONS WITH EXPERIMENTAL COMPARISONS[1]

H.M. Glaz
Applied Mathematics Branch
Naval Surface Weapons Centre
White Oak, Silver Spring, MD 20910

Phillip Colella
Lawrence Berkeley Laboratory
University of California
Berkeley, California 94720

I.I. Glass
Institute for Aerospace Studies
University of Toronto
Toronto, Canada

R.L. Deschambault
Institute for Aerospace Studies
University of Toronto
Toronto, Canada

August 1984

---

[1] Supported in part by the Applied Mathematical Sciences subprogram of the Office of Energy Research, U.S. Department of Energy under contract DE-AC03-76SF00098.

A numerical study of oblique-shock-wave reflections with experimental comparisons

By H. M. Glaz*, P. Colella[+], I. I. Glass[+] and R. L. Deschambault[+]

*Applied Mathematics Branch, Naval Surface Weapons Centre,
White Oak, Silver Spring, MD 20910, U.S.A.
[+]Mathematics Department, Lawrence Berkeley Laboratory
Berkeley, CA 94720, U.S.A.
[+]Institute for Aerospace Studies, University of Toronto,
Toronto, Canada.

A direct comparison is made for several cases of oblique-shock-wave reflections between interferometric results obtained at the University of Toronto, Institute for Aerospace Studies (UTIAS) 10 x 18 cm Hypervelocity Shock Tube and numerical results obtained using a state-of-the-art computational method for solving the Euler equations. Very good qualitative agreement is obtained for equilibrium and frozen flowfields except in small regions for which the experiments were dominated by viscous flow. The quantitative agreement is very close in some cases but can be off by 10-15% in cases with nonequilibrium flow and/or viscous structures. Additional parametrized sequences of calculations are presented in order to assess the utility of the present numerical method in constructing the various reflection - transition-lines for perfect inviscid flows in the shock-wave Mach-number, wedge-angle (M_S,θ_W)-plane, and the validity of the "boundary-layer defect" theory.

1. Introduction

In the past several years, substantial advances have been made in the numerical analysis of hyperbolic equations of motion, especially the equations of nonstationary gasdynamics. It is now possible to routinely apply the resulting computer codes on problems which involve complex physical phenomena such as flows with multiple shock waves and slipstreams.

Several questions arise from such work. First, how accurate are the numerical results in reproducing solutions of the Euler equations?

In particular, to what extent does the truncation error inherent in a numerical method alter the system of equations being solved? For example, large amounts of artificial viscosity can effectively produce a solution to a parabolic approximation of the Euler equations, but not a solution to the Navier-Stokes equations, and completely miss the fine structure of wave interactions. Second, how well do such results compare with experimental data (which deals with real flows, including viscous effects) in the event that such data are available?

Reliable numerical results are needed for a wide variety of nonstationary compressible-flow problems in shock-wave dynamics, explosion-implosion dynamics and elsewhere; in some cases, there are virtually no experimental data available for analysis. This creates the requirement for a benchmark problem which contains sufficiently complex nonlinear wave interactions to truly validate a computer code and yet is amenable to accurate experimental measurement. The problem of nonstationary oblique-shock-wave reflections from a compressive corner in various gases is currently the strongest candidate to play this role. The complex wave structure in the Mach-stem region of such flowfields closely resembles the flowfield phenomenology in typical applications (e.g., a spherical explosion reflecting off an ideal surface). During the past five years, extensive experimental and analytical data were obtained for these problems (Ben-Dor and Glass 1979, Ben-Dor and Glass 1980, Ando and Glass 1981, Lee and Glass 1982, Shirouzu and Glass 1982, Deschambault and Glass 1983, Deschambault 1984, Hu and Glass 1984, Hu 1984, Hu and Shirouzu 1984, Wheeler and Glass 1984, Wheeler 1984). Additionally, analytic and experimental work has been ongoing in this area since Mach 1878, and especially since the work of von Neumann 1943 on shock-wave theory for gases.

In their comparison of experimental and computational results for this problem, Ben-Dor and Glass 1978, and Deschambault and Glass 1983 concluded that advances in numerical technique would be required before numerical results could be viewed with the same confidence as experimental data. In particular, they found that computer codes were able to correctly obtain the overall reflection pattern but gave poor agreement with interferometric data concerning the detailed structure of the isopycnics (lines of constant density) of the disturbed flowfield behind the reflected shock. Many of these computational results were underresolved due to the constraints of the then existing computer technology, where the results presented here are fully resolved because they were obtained with a state-of-the-art, low diffusion scheme on a modern computer, taking full advantage of the computer's vector processor. The main objective of this paper is to change this assessment and place the numerical analysis of perfect inviscid compressible flow on an equal footing with experimental methods. The present study will demonstrate this by comparison of the numerical with the experimental results for argon and air.

Such comparisons are complicated by the fact that the flowfields under investigation are not ideal due to the following phenomena. A boundary layer is induced behind the shock-wave system on the wedge surface. This not only alters the interaction of the slipstreams with the wall but the transition boundary between regular and Mach reflection due to von Neumann 1943. The slipstream is not an ideal contact surface between thermodynamically different states; it spreads and thickens and undergoes transition from a laminar to a turbulent state. In addition, the second shock wave in double-Mach reflection is non-uniform in strength from the second triple point to the first slipstream (Fig. 1). The interaction between this shock wave and the slipstream is also not well understood. The shock becomes a compression wave as it interacts with the slipstream, which remains stable despite the pressure gradient imposed on it. No reflected expansion waves are observed that might neutralize this gradient as in a steady supersonic jet outflow. No waves can directly enter from the slipstream into the uniform region behind the Mach stem since the flow there is subsonic. Finally, the perfect (frozen) flows in air become excited and may be in nonequilibrium or equilibrium states. This complicates the numerical analyses which now require complex equations of state for equilibrium flows or rate equations for the excitation of the internal degrees of freedom such as dissociation and ionization for nonequilibrium flows at high initial shock-wave Mach numbers.

2. Oblique-shock-wave reflections

The four types of pseudo-stationary oblique-shock-wave reflection patterns are shown in Figure 1 and consist of (a) regular reflection-RR, (b) single Mach reflection-SMR, (c) complex Mach reflection-CMR, and (d) double Mach reflection-DMR. Figure 1 illustrates the definitions of wedge angle θ_W, triple-point trajectory angles, χ,χ', various shock waves I,R,R',M,M', slip surfaces S,S' and the flow regions (1) - (5) produced by RR, SMR, CMR and DMR reflections. The angle δ between the incident I and reflected R shock waves is also shown as well as the angle ω' between R and the wall or R and the triple-point trajectory χ. The bow shock standoff distance s, and the length L, between the wedge corner and the reflection point or Mach stem are also indicated. Such quantities can be measured experimentally and predicted numerically and provide important information on the state of the gas (frozen, nonequilibrium or equilibrium), (Shirouzu and Glass 1982, Hu 1984, and Hu and Glass 1984).

If real-gas and viscous effects can be ignored, the problem has no intrinsic length-scale, suggesting the use of the self-similar or pseudo-stationary coordinate system $(\xi,\eta) = ((x-x_0)/(t-t_0), (y-y_0)/(t-t_0))$ where (x_0,y_0) are the coordinates of the wedge corner and t_0 is the time at which the incident shock wave reaches the corner. Jones et al. 1951 show that the nonstationary Euler equations referred to this coordinate system transform into the steady Euler equations with the additon of source terms. We remark that the ratio s/L is constant for self-similar solutions of the nonstationary equations, just as s is constant for steady supersonic flow. In this and other ways a change of pseudo-stationary coordinates is very useful in the analysis of these flowfields and will be used in this study.

In particular, the type of reflection pattern is a function of the incident shock-wave Mach-number M_S, the wedge angle θ_w, and the gas equation-of-state. The transition boundaries in the (M_S,θ_w)-plane for oblique-shock-wave reflection are reproduced from Lee and Glass 1982 in Figure 2, for real air and a polytropic equation-of-state with $\gamma=1.40$. The analogous figure for argon ($\gamma=5/3$) may be found in this reference. The construction of the transition lines is based on various (heuristic) transition criteria and the numerical calculation of the jump-conditions at reflection and triple points. These criteria, which have been the subject of extensive investigation in the literature, are summarized in Lee and Glass 1982 and Shirouzu and Glass 1983. In Section 5, the numerical results will be used to partially assess the validity of some of these criteria as well as the overall accuracy of the transition diagram, Figure 2.

The fourfold partition of the (M_S,θ_w)-plane illustrated in Figure 2 is quite coarse relative to the rich phenomenology present in these flowfields. Some other features which may be similarly partitioned (see Ben-Dor and Glass 1979) are (a) whether or not the reflected shock is detached or attached to the wedge corner, (b) in the attached case, whether the flow at the corner is subsonic or supersonic, (c) for RR, whether the flow is subsonic or supersonic, in pseudo-stationary coordinates, at the reflection point, and (d) for CMR and DMR, whether or not M "toes-out" or "toes-in".

A comprehensive study of these issues is beyond the scope of of this paper, but they will be discussed as appropriate in the comparison of experimental and numerical results in Section 5.

3. Experimental techniques

The experiments for this study were performed in the University of Toronto, Institute for Aerospace Studies (UTIAS) 10 x 18cm Hypervelocity Shock Tube. Background on the performance and operation of the shock tube can be found in Boyer 1964, with the details of the experiments in Deschambault 1984. The facility includes specialized instrumentation used to observe density and pressure in the complex flow fields generated in the present experiments.

The shock tube test section is equipped with large high-quality interferometric windows. To study the density distributions of the flow fields a 23-cm dia. field of view Mach-Zehnder interferometer was employed. The specifications and operating instructions for this instrument can be found in Hall 1954. The interferometer was used in the infinite-fringe mode which allows the direct observation of isopycnics (lines of constant density) in the two-dimensional flow field. The light source employed was a giant-pulse ruby laser which enabled the recording of dual-wavelength (694.3 nm and 347.2 nm) infinite-fringe interferograms, with an exposure time of 30 ns. The test gases used in the present work were argon and medical-grade air.

The reflection patterns were produced by the impingement of a normal shock wave with steel wedges. Both cold-gas (CO_2 driver) and combustion-driver techniques were used to produce the incident shock waves into the test gases used in the present study. For further discussion of the facility and error of measurement associated with the instrumentation see Deschambault 1984 and Glaz et al. 1984.

For some of the experimental results presented here, it was necessary to use test gases with very low densities and pressures relative to atmospheric conditions. As a result, vibrational nonequilibrium effects must be taken into account in analyzing the corresponding interferograms. We note here that it is easy to check for a relaxation zone behind the incident shock wave because such a zone will produce extra fringes parallel to the shock in the post-shock flowfield. Behind the reflected shock wave, the characteristic signature of a relaxing gas is the degree of tangential incidence of the isopycnics with the reflected shock wave.

4. Numerical Method

The numerical results presented in this paper have been calculated with a version of the Eulerian second-order Godunov scheme for nonstationary gasdynamics of a type considered by Colella and Woodward 1984. The version of the scheme used here is presented in Colella and Glaz 1982, 1983, including the modifications required for nonpolytropic gases.

The method is a finite-difference scheme for systems of hyperbolic conservation laws in one spacelike dimension; for multidimensional applications such as the shock-on-wedge problem, we employ operator splitting. Differencing is in conservation form and the numerical fluxes are computed by solving zone interface Riemann problems whose time-centered left and right states are computed from the characteristic form of the equations. This technique leads to second-order accuracy in smooth flow and insures that the method is upstream-centered. In practice, the method is very stable and robust. In the immediate vicinity of a strong shock, some dissipation is required; this has been accomplished by smoothly degrading the scheme to the first-order Godunov scheme in such region The degree of degradation is a function of the shock width and strength.

For the argon cases, we have used a perfect (frozen) gas equation-of-state with $\gamma=5/3$. If the shock tube test gas was real air, the equation-of-state was chosen to be either a perfect (frozen) gas with $\gamma=7/5$ or the Hansen 1959 real air equation-of-state as modified by Deschambault 1984 for the present application. The efficient solution of the Riemann problem in the context of our second-order Godunov method for an arbitrary equation-of-state is treated in Colella and Glaz 1982, 1983. Also, these papers demonstrate that the choice of equation-of-state has a substantial influence on the quantitative numerical results, as might be expected.

As noted in the preceding section, vibrational nonequilibrium (which is only temperature dependent) can be significant for moderate to high Mach numbers when the test gas is air (at high Mach numbers dissociation effects are also density dependent); for the argon cases considered here, we expect the gas to remain frozen. The choice of an appropriate equation-of-state for the air calculations depends mainly on the vibrational relaxation length, ℓ_V, behind the shock-waves I,R,M of Figure 1. If $\ell_V \geq \ell$ (where ℓ is a characteristic flow length arising in the problem), then the gas is frozen and the perfect gas equation-of-state is correct. If $\ell >> \ell_V$, then the gas is in equilibrium and the Hansen equation-of-state for real air is used. Finally, if $\ell_V \sim \ell$, then neither the frozen nor the equilibrium hypothesis is appropriate, and the flow is said to be in nonequilibrium. We have numerically treated such cases as equilibrium flowfields using the Hansen equation-of-state, although the only correct procedure would be to solve an additional partial-differential equation representing a rate equation for vibrational relaxation (and for dissociation at high Mach numbers). This decision will be an important issue in our discussion of these cases in Section 5.

The computational mesh and our problem initialization procedure is illustrated in Figure 3. Note that these figures are drawn from right to left so as to conform with the experimental interferograms. We have used a square (i.e., $\Delta x = \Delta y =$ constant) mesh for all of the computations in Section 5. Since the flow is pseudo-stationary, the choice of Δx is immaterial; however, in those cases for which a comparison of pressure-gauge records was desirable (see Glaz et al. 1984), the total length should be chosen appropriately.

The initial data is $\underline{U}_0$, M_s where $\underline{U} = (\rho, p, u, v)^T$ is the state vector and M_s is the initial shock-wave Mach-number. From these data and the given equation-of-state, the post-shock state $\underline{U}_1$ may be calculated. To initialize the two-dimensional calculation, these data are placed on the grid far upstream (~60-75 zones) of the corner, as illustrated in Figure 3a; interpolation of conserved quantities [i.e., $\underline{U}^c = (\rho, \rho u, \rho v, \rho E)^T$] is used for zones which straddle the incident shock. However, this is a very poor representation of the numerical shock since any shock capturing scheme will diffuse a shock wave over two or more zones in the computational mesh. The resulting structure is referred to as a discrete travelling wave (i.e., a mesh function which depends only on $\underline{x}-\underline{V}t$, where $\underline{V}$ is the vector velocity of the wave and equals the shock speed in magnitude for a discrete shock wave). Starting with any initial data (e.g., the one zone $\underline{U}_0$ - $\underline{U}_1$ jump described above) satisfying the Rankine-Hugoniot conditions, the solution will tend as the number of times steps becomes large towards the appropriate discrete travelling wave, plus other low-amplitude waves which we refer to as "starting error", with the starting error separating from the travelling wave. For the present application, it is very important to insure that the starting error is eliminated before the shock wave is allowed to reflect, and we proceed as follows. First, the computer code is allowed to run until the shock wave reaches the corner, and the situation in Figure 3b is reached. In this figure, the region immediately behind the shock and about 2-3 zones thick is the discrete travelling wave and the small (<5%) relative amplitude disturbances further downstream is the one-time starting error. The computer code then arbitrarily changes the flowfield to that illustrated in Figure 3c, i.e., the discrete travelling wave (arbitrarily set to exactly 4 zones in the computer code) is retained but the starting error is replaced by the post-shock state $\underline{U}_1$.

At this point, the flowfield becomes truly two-dimensional and the computer code is now run without further interruption until the end of the calculation is reached.

The boundary conditions for this problem, which are standard, are discussed in detail in Colella and Glaz 1983. We remark here that our treatment of the intersection of the incident shock with the upper and/or left-hand boundary is not entirely consistent with the discrete travelling wave and leads to the introduction of a low relative amplitude (~1%) wave behind the incident shock at it's intersection with the boundary. This wave, which we refer to as a boundary error, may lead to a rather unaesthetic structure in the contour plots and it can impinge on the disturbed flowfield behind the reflected shock. Examples will be noted in Section 5.

All calculations were performed on a CRAY I at Los Alamos National Laboratory, Los Alamos, New Mexico. The computer code was designed to take significant advantage of the machine's vector architecture. Each calculation in Section 5 required 15-40 minutes CP time with most in the range of 20-30 minutes. Much of this time is wasted on the extra grid points introduced to eliminate the starting error as well as grid points outside the reflected shock. Also, a fine mesh is only really needed in the Mach stem region. Thus, an intelligent adaptive mesh structure could reduce these timings substantially.

5. Computational results

A direct comparison of experimental results and numerical calculations is presented in Part I of this section for five cases. In Part II, the results of a parametrized sequence of calculations are presented in order to demonstrate the capability of our numerical method to compute transition boundaries in the (M_S,θ_W)-plane. An additional sequence is presented to demonstrate (upon comparison with experimental data) the effect of boundary-layer displacement on the RR$\rightleftharpoons$DMR transition.

I. Comparison of Experiment with Calculation

The initial conditions for the five cases are listed in Table I along with the computational mesh (NX,NY) and the equation-of-state (EOS) selected for each calculation. All four wave configurations are represented in the range of (M_S,θ_W) considered. The following data are presented for each case: experimental isopycnics, computed isopycnics using the same density levels as were obtained in the experiment, computed isopycnics using 30-contour levels equally spaced between the extreme flowfield densities, and a wall-density distribution plot (ρ/ρ_0 vs. x/L) containing both the numerical and experimental results. Numerically generated contour plots (with 30 equally spaced contour levels) of other flowfield quantities will occasionally be included in the discussion. Of particular interest is the Mach number in pseudostationary coordinates, $\tilde{M}$, defined by $\tilde{M}^2(x,y,t) = [(u-\xi)^2 + (v-\eta)^2]/a^2$ where a = sound speed. The quantity $\tilde{M}$-1 is plotted so that the zero-contour-level corresponds to the sonic line in this coordinate system.

<u>Case 1:</u> RR, $M_S = 2.05$, $\theta_W = 60^\circ$, argon. Comparison of the experimental and numerical isopycnics (Figs. 4a,b) show them to be in good agreement with an error of about one fringe at the start of the subsonic region. The wall density distribution (Fig. 4d) disagrees by about the same amount. It may be observed in Fig. 4c that the contour levels curve sharply towards the

reflection point just above the wedge surface, an effect which is not present in the experimental results. This numerical error is referred to as "wall heating" and is commonly observed in shock capturing calculations as shown, for example, in Noh 1976. Wall heating affects only the density, temperature, etc., but not the pressure (Fig. 4e). It may be seen to account for part of the observed error in this case, including the slight error in the value of the reflected shock wave density ρ_2 on the wall. In addition, the error in the stand-off distance of the bow shock s, relative to the experimental distance from the reflection point P to the corner L, is about 6.2%.

Case 2: SMR, $M_S = 2.03$, $\theta_w = 27^\circ$, air. The agreement for this case is extremely strong in all respects (Figs. 5a,b,c,d). Quantitatively, the isopycnics are off by about one fringe (Figs. 5a,b), and the wall-density plot (Fig. 5d) shows similar agreement for its entire length. Note that the contact discontinuity spreads out in the experiment and, consequently, does not roll up as much as in the calculation.

Case 3: CMR, $M_s = 10.37$, $\theta_w = 20^\circ$, air. The experimental results (Fig. 6a) show very strong nonequilibrium effects in the disturbed flowfield behind the reflected shock, with an almost equilibrium incident shock. The wedge surface does not appear straight owing to diffraction effects indicating that the sidewall boundary layer is significant. We get reasonably good qualitative agreement in the isopycnic patterns (Figs. 6a,c) although the tangential incidence at the shock in Fig. 6a cannot appear in Fig. 6c. Also, the numerical wall heating is substantial. The quantitative agreement is equally good (Figs. 6a,b). In evaluating the wall-density plot (Fig. 6d), we note that the data points were evaluated assuming frozen-triple-point conditions. Also, we measure $\chi = 12.5^\circ - 13.25^\circ$, 15.3° and the attachment angle = $20^\circ - 21^\circ$, 25.5° for the experiment and calculation, respectively. The latter difference explains the disagreement in Fig. 6d near $x/L = 1.0$. If the vortex roll up patterns could be lined up and the Hansen equation-of-state used in evaluating the data, it seems that quite good quantitative agreement could be obtained for x/L small despite the wall heating error. The dip in Fig. 6d at $x/L \sim 0.25$ is due to the boundary error.

Case 4: CMR/DMR, $M_s = 7.19$, $\theta_w = 20^0$, air. The experimental isopycnics (Fig. 7a) show clearly that this flowfield is neither frozen nor in equilibrium. Also, the isopycnics leave the reflected shock almost tangentially which indicate that there are substantial nonequilibrium effects across this wave as well. A more detailed discussion of equation-of-state and nonequilibrium effects in the numerical analysis of this case is available in Colella and Glaz 1983. For the equation-of-state used here, the triple-point angle is in exact agreement. Note that ρ_3/ρ_0 is in very poor agreement (Fig. 7d) because the experimental data reduction used the frozen-triple-point conditions. The otherwise excellent agreement for $x/L<0.15$ is surprising in view of the strong nonequilibrium and viscous effects in this region. The contours, including the vortex pattern, are in excellent qualitative and quantitative agreement (Figs. 7a,b,c). The attached corner is subsonic in the experiment (Fig. 7a) and supersonic in the calculation (Figs. 7 b,c). This disagreement is caused by the nonequilibrium effects as may be noted by comparing numerical results for different choices of equation-of-state, Colella and Glaz 1983. The $\tilde{M}$ contours (Fig. 7e) show the sonic line approaching the kink which corresponds to this case lying on the CMR/DMR transition boundary; Lee and Glass 1982 conjecture that this transition occurs when the sonic line reaches the kink. This case is an excellent example of the computational boundary error's effects on the disturbed flowfield (Figs. 7b,c and 7,d, $x/L \sim 0.35$).

Case 5: DMR, $M_s = 8.7$, $\theta_w = 27^{\circ}$, air. Figure 8a exhibits substantial nonequilibrium effects. In particular, $\ell_v \sim 0.2$ x/L for the incident shock and the isopycnics are at tangential incidence to the reflected shock. Also, the relaxing gas in the Mach stem region has obscured the slipstream and part of the roll-up pattern. Comparison of Figs. 8a,c show very good agreement. The roll-up pattern agrees very well, although the slipstream normal to the wall at x/L $\sim$ 0.02 and the backward facing shock normal to the wall at x/L $\sim$ 0.065 in Fig.8c are either not resolved or are lost due to viscous effects in Fig. 8a. Details of the calculated flowfield in the Mach stem region are presented in Figs. 8e,f,g. The existence of an extra pseudostationary stagnation point at the intersection of two slipstreams is noted in Fig. 8e. WE have measured $\chi = 9.6^{\circ}$, 7.0° and R ($\equiv$ ratio of th distance between the two triple points and L) = 0.1854, 0.1769 for the calculatio and experiment, respectively. The data points in Fig. 8d near x/L = 0.0 were obtained using the triple-point conditions for $\gamma = 1.40$ and $\chi = 7.0^{\circ}$. The measured corner-attachment angles are 33.5°, 23.0° for the calculation and experiment, respectively. This nonequilibrium effect (which apparently is poorly modelled with the equilibrium Hansen equation-of-state) explains the disagreement near x/L = 1.0 in Fig. 8d. We note that the numerical thermal layer is a large effect for this problem. Overall, real-gas effects have an extensive impact on the flow dynamics for this case and the equilibrium calculation cannot reproduce these effects.

II. Transition Sequences

We have calculated a sequence of cases for perfect air at $\theta_w = 45^{\circ}$ for $1.3 \le M_s \le 2.6$ in increments of $\Delta M_s = 0.1$. Due to lack of space, only a small portion of the results will be presented here. The full study, as well as the calculations for other line segments in the (M_s, θ_w)-plane are included in Glaz et al. 1984. The purpose of these calculations is to demonstrate the feasibility of using the computer code to construct the inviscid transition lines in the (M_s,θ_w)-plane and to test transition theories based on inviscid arguments.

The contours of constant density for the $M_s = 1.70$ case are shown in Figure 9a. The configuration can be seen to be near the SMR $\rightleftarrows$ CMR boundary, but is is difficult to precisely judge the shape of the reflected shock. Contours of constant self-similar Mach number in the vicinity of the triple point are shown for the case and for $M_s = 1.80$ in Figure 9b,c. The sonic line (in pseudostationary coordinates) has moved into Region 2 for the $M_s = 1.80$ case; the extent of the supersonic region increases with increasing shock-wave Mach number, $M_s \geq 1.80$ (not shown). Assuming that the SMR $\rightleftarrows$ CMR transition occurs when Region 2 becomes supersonic at the triple point (see Lee and Glass 1982), it follows that the $M_s = 1.80$ case is a CMR. Similarly, we find that the cases for $1.3 \leq M_s \leq 1.7$ are SMR's, because Region 2 is entirely subsonic for these results (not shown). Therefore, the computer code predicts the 45°, perfect gas SMR CMR transition to lie in the range $1.70 \leq M_s \leq 1.80$. We remark that the analogous calculations for 45°, imperfect air with the Hansen equation-of-state (not shown) predicts $1.60 \leq M_s \leq 1.70$ for the same transition. Both results reasonably agree with Fig. 2, but the Hansen results are in better agreement. A more precise prediction would simply be a matter of choosing a smaller value of ΔM_s and, perhaps, using more mesh points in the triple point region to improve resolution.

The results for the weak DMR case, $M_s = 2.30$, are shown in Figure 9d,e. One theory for the CMR $\leftrightarrows$ DMR transition (see Lee and Glass 1982) is that the flow at the first triple point should be supersonic with respect to the motion of the kink. Since the flow immediately beneath the reflected shock and between the two triple points is constant, this criterion is equivalent to requiring that the sonic line (in pseudo-stationary coordinates) intersect the kink. Also, the sonic line should have the same tangent at the kink as the second Mach stem, because the flow is supersonic ahead and subsonic behind this discontinuity. Using this criterion, the calculations show that the $M_S = 2.30$ case is a weak DMR but that the cases for which $1.70 \le M_S \le 2.20$ are CMR's, in reasonable agreement with Figure 2. We remark that 45°, imperfect air calculations (not shown) are in somewhat better agreement.

Another sequence of cases for perfect argon with $M_S = 7.10$ has been calculated for various choices of θ_W with $49^{\circ} \le \theta_W \le 54^{\circ}$. The purpose of these calculations is to estimate the inviscid RR$\rightleftharpoons$DMR transition boundary and, by comparison with experimental results, to demonstrate and quantify the well-known disagreement between theory and experiment for this issue (see, for example, Shirouzu and Glass 1982).

The experimental and computational double-Mach-reflection configurations for $\theta_W = 49^{\circ}$ are shown in Figures 10a,b. These results are in substantial disagreement concerning the extent of the Mach stem region relative to the entire flowfield. The computational results for $\theta_W = 53.2^{\circ}$ are shown in Figure 10c; this case is in much closer agreement with the experiment at $\theta_W = 49^{\circ}$ than is Figure 10b. The difference, $\Delta\theta_W \sim 4.0 - 4.5^{\circ}$, may be viewed as the "boundary-layer defect" (see Taylor and Hornung 1982, Shirouzu and Glass 1982, and Wheeler and Glass 1984). We have attempted to calculate the precise RR$\rightleftharpoons$DMR transition point by plotting the height of the Mach stem relative to L vs. θ_W for several computations in Figure 10d and extrapolating the curve to zero height. The result is $\theta_W \sim 53.85^{\circ}$, which disagrees moderately with the theoretical result of $\theta_W \sim 54.4^{\circ}$ in Lee and Glass 1982. We remark that this error may be caused by an unnoticed bias in our measuring technique (simply using a ruler on the computer-generated contour plots of the blow-up Mach stem region), lack of numerical resolution when the Mach stem is only 1-2 zones high, or a numerical error in the post-shock flowfield at the wall. In any case, the error is small relative to the viscous-inviscid difference and it is also possible that the theoretical inviscid prediction, which is an infinitesimal result, of $\theta_w \sim 54.4^o$ does not apply when the entire disturbed flowfield is taken into account.

6. Conclusions

A computer code has been developed for the inviscid, perfect-gas shock-on-wedge problem and the results have been compared with the best available experimental data. The code is based on state-of-the-art methodology and has only recently been available.

Good to excellent qualitative agreement has been obtained in all cases, and this applies to structures beneath the reflected shock such as the vortex roll-up as well as coarser criteria such as the reflection pattern. Nonequilibrium effects and viscous structures may at least be strongly suspected to cause any of the qualitative disagreements. Quantitatively, the results are very good for flow fields without observable nonequilibrium or viscous effects. When such effects are significant, errors of 10-15% are typical. A pervasive, but easily analyzable, numerical error present in most cases is the "wall-heating" effect.

Although the case has not been entirely proven, it appears that the computer code represents a substantial predictive capability for the shock-on-wedge problem restricted to inviscid, perfect gases. Even for viscous, real-gas flowfields, the computational results provide a significant amount of information, including highly resolved flowfield structures.

Significant nonequilibrium and viscous effects have been demonstrated in the shock-wave diffraction experiments. Much of this could be inferred without the numerical study, but the latter can provide a quantitative estimate of the various effects. In particular, vibrational relaxation is observed in the high shock-wave Mach-number cases, and this can have large-scale effects on criteria such as the corner attachment angle and type (subsonic or supersonic) and viscous effects are important in determining the vortex roll-up pattern and the wedge corner flowfield. Although these effects occur in thin layers or small regions, they may have an effect on the quantitative results in the inviscid portion of the flowfield.

The capability of the computer code to discriminate between very small increments in problem parameters (M_S, θ_W, and the equation-of-state, although the latter has not been treated here) has been demonstrated. Using parametrized sequences of calculations, it would be possible to construct transition boundaries in the (M_S,θ_W)-plane. Of course, the transitions obtained would be dependent on the transition criteria used in their construction; our use of the sonic criterion in self-similar coordinates shows how the infinite amount of data potentially available from a calculation can be invaluable in evaluating one of the proposed criteria.

Also, we have been able to validate the conjecture that the RR$\leftrightarrows$DMR transition is offset in experiments by a boundary-layer defect.

In future work, we intend to modify our computer code and include an approximation for vibrational relaxation. We expect that this work will settle some of the questions raised in this paper. The results presented here demonstrate, however, that a valid approximate solution method for the Navier-Stokes equations will be required if complete agreement between experiment and calculation is demanded. Despite these shortcomings, the comparison of the present numerical simulations with interferometric data from RR, SMR, CMR and DMR experiments are probably the best available to date. Additional results are available in Glaz et al. 1984.

We are grateful to Mr. Ralph Ferguson for his extensive programming work for these calculations. The discussions with Dr. George Ullrich and Dr. Allen Kuhl are very much appreciated.

The financial assistance received from the U.S. Department of Energy at the Lawrence Berkeley Laboratory under Contract DE-AC03-78SF00098; from the U.S. Defense Nuclear Agency under DNA Task Code Y99QAXSG; from the Naval Surface Weapons Center Independent Research Fund; from the U.S. Air Force Office of Scientific Research under Grant 82-0096; and from the Natural Science and Engineering Research Council of Canada is acknowledged with thanks.

References

Ando, S. & Glass, I. I., Proc. 7th Int. Symp. on the Military Applications of Blast Simulation, 1981.

Ben-Dor, G. & Glass, I. I., AIAA J., V. 16, p. 1146 (1978).

Ben-Dor, G. & Glass, I. I., J. Fluid Mech. 92, (1979), pp. 459-496.

Ben-Dor, G. & Glass, I. I., J. Fluid Mech. 96, (1980), pp. 735-756.

Boyer, A. G., Univ. of Toronto, UTIAS Rep. No. 99, 1964.

Colella, P. & Glaz, H. H., Proceedings, Eighth International Conference on Numerical Methods in Fluid Dynamics, Aachen, 1982, ed. E. Krause, Springer-Verlag.

Colella, P. & Glaz, H. M., Lawrence Berkeley Laboratory Report LBL-15776, November 1983.

Colella, P. & Woodward, P. R., J. Comput. Phys., to appear 1984.

Deschambault, R. L. & Glass, I. I., J. Fluid Mech. 131 (1983), pp. 27-57.

Deschambault, R. L., Univ. of Toronto, UTIAS Rep. No. 270, January 1984.

Glaz, H. M., Colella, P., Glass, I. I. & Deschambault, R. L., UTIAS Report No. 285, 1984.

Hall, J. G., Univ. of Toronto, UTIAS Rep. No. 27, 1954.

Hansen, C. F., NASA TR R-50, 1959.

HORNUNG & TAYLOR 1982

Hu, J. T. C., UTIAS TN No. 253, 1984.

Hu, J. T. C. & Glass, I. I., paper to be published in 1984.

Hu, J. T. C. & Shirouzu, M., UTIAS Report No. 283, 1984.

Jones, D. H., Martin, P. M. E. & Thornhill, C. K., Proc. Roy. Soc. A209, (1951), pp. 238-247.

Lee, J.-H. & Glass, I. I., Univ. of Toronto Institute for Aerospace Studies Report No. 262, June 1982.

Mach, E., Akad. Wiss. Wien, 77, (1878), II, pp. 819-838.

von Neumann, J., Explosives Research Report No. 12, Navy Dept., Bureau of Ordnance, Re2C, Washington, D.C., 1943.

Noh, W. F., Lawrence Livermore National Laboratory Report UCRL-52112, June 1976.

Shirouzu, M. & Glass, I. I., University of Toronto Institute for Aerospace Studies Report No. 264, November 1982.

Wheeler, J., UTIAS Tech. Note No. 256, 1984.

Wheeler, J. & Glass, I. I., paper to be published in 1984.

TABLE I. EXPERIMENTAL AND NUMERICAL INITIAL CONDITIONS

Case	Gas	Type	θ_w	M_s	P_0(kPa)	ρ_0(kg/m^3)	EOS	NX	NY
1	Argon	RR	60^0	2.05	20.0	$3.23\text{x}10^{-1}$	$\gamma=5/3$	355	90
2	Air	SMR	27^0	2.03	33.3	$3.87\text{x}10^{-1}$	$\gamma=7/5$	350	130
3	Air	CMR	10^0	10.37	6.7	$7.53\text{x}10^{-1}$	Hansen	400	140
4	Air	C/DMR	20^0	7.19	8.0	$9.29\text{x}10^{-2}$	Hansen	420	220
5	Air	DMR	27^0	8.70	4.1	$4.76\text{x}10^{-2}$	Hansen	440	85

Figure Captions

1. Schematic diagrams of types of oblique-shock-wave reflections; a) RR, b) SMR, c) CMR and d) DMR; also definitions of L and s.

2. Regions of RR, SMR, CMR and DMR and their transition boundaries in the (M_s, θ_w)-plane for perfect (frozen) air ——— and imperfect (equilibrium) air ------, $p_0 = 2.00$ kPa, $T_0 = 300$K, $\gamma = 1.40$.

3. Numerical scheme for flow initialization; a) Starting procedure, b) Shock reaching corner, c) Elimination of small disturbances.

4. Case 1, RR, $M_s = 2.05$, $\theta_w = 60°$, $p_0 = 20.0$ kPa, $T_0 = 297.6$ K, argon, $\rho_0 = 0.323$ kg/m^3; a) Interferogram and experimental isopycnics, b) Numerically simulated isopycnics shown in a), c) 30 numerical isopycnics, equally spaced between the minimum and maximum flowfield densities, d) Wall-density distribution; ——— computational results, ● experimental data, e) 30 equally spaced numerical isobars.

5. Case 2, SMR, $M_s = 2.03$, $\theta_w = 27°$, $p_0 = 33.3$ kPa, $T_0 = 299.2$ K, air, $\rho_0 = 0.387$ kg/m^3; a) Interferogram and experimental isopycnics, b) Numerically simulated isopycnics shown in a), c) 30 equally spaced numerical isopycnics, d) Wall-density distribution; ——— computational results, ● experimental data.

6. Case 3, CMR, $M_s = 10.37$, $\theta_w = 10°$, $p_0 = 6.7$ kPa, $T_0 = 299.0$ K, air, $\rho_0 = 0.753$ kg/m^3; a) Interferogram and experimental isopycnics, b) Numerically simulated isopycnics shown in a), c) 30 equally spaced isopycnics, d) Wall-density distribution; ——— computational results, ● experimental data.

7. Case 4, C/DMR, $M_s = 7.19$, $\theta_w = 20°$, $p_0 = 8.0$ kPa, $T_0 = 298.5$ K, air, $\rho_0 = 0.0929$ kg/m^3; a) Interferogram and experimental isopycnics, b) Numerically simulated isopycnics shown in a), c) 30 equally spaced isopycnics, d) Wall-density distribution; ——— computational results, ● experimental data, e) 30 $\tilde{M}$ contour levels (blowup frame); minimum and maximum $\tilde{M}$ values are relative to the frame.

8. Case 5, DMR, $M_s = 8.70$, $\theta_w = 27°$, $p_0 = 4.1$ kPa, $T_0 = 299.2$ K, air, $\rho_0 = 0.0476$ kg/m^3; a) Interferogram and experimental isopycnics, b) Numerically simulated isopycnics shown in a), c) 30 equally spaced isopycnics, d) Wall-density distribution; ——— computational results, ● experimental data, e) Density contours (blowup frame), f) Pressure contours (blowup frame), g) $(\bar{u}, \bar{v})$-vector plot (blowup frame plus overlay of wave system).

9. Transition sequence for perfect (frozen) air, $\theta_w = 45°$; a) isopycnics, $M_s = 1.70$, $\theta_w = 45°$, b) $\tilde{M}$ blowup for $M_s = 1.70$, showing sonic line interior to the reflected shock, c) $\tilde{M}$ blowup for $M_s = 1.80$, showing region of supersonic flow beneath the reflected shock, d) isopycnics, $M_s = 2.30$, $\theta_w = 45°$, DMR, e) Blowup showing details of $\tilde{M}$ for case d) above, where sonic line intersects the kink.

Figure Captions (continued)

10. Transition sequence for argon, $M_S = 7.1$; a) Interferogram and experimental isopycnics, $M_S = 7.1$, $\theta_w = 49.0°$, $p_0 = 2.0$ kPa, $T_0 = 296.3$ K, $\rho_0 = 0.0329$ kg/m^3, b) 30 equally spaced isopycnics, $\theta_w = 49.0°$, c) 30 equally spaced isopycnics, $\theta_w = 53.2°$, d) Plot of DMR Mach stem height versus θ_w, extrapolated to zero height for RR ($h/L = 0$ for $\theta_w = 53.85°$), $h/L = 0$ for $\theta_w = 54°$ is a numerical result. ▲ experimental point, ● numerical results.

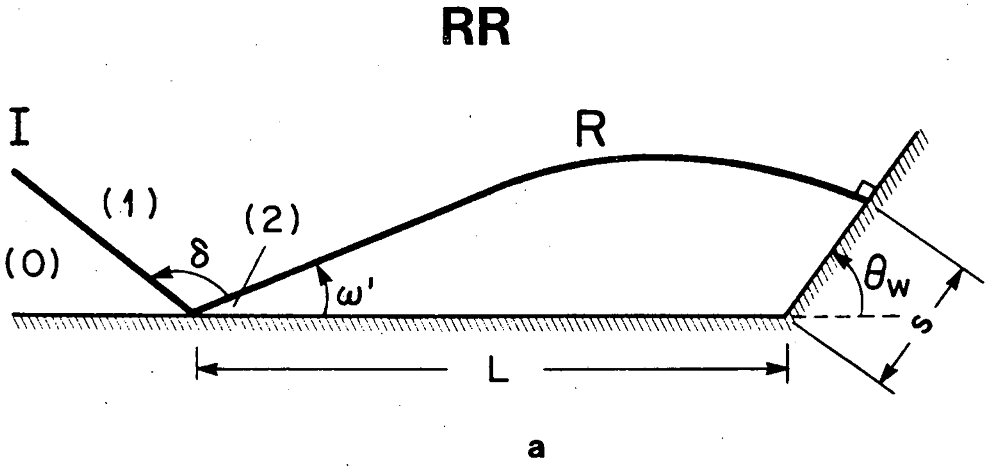

Figure 1a

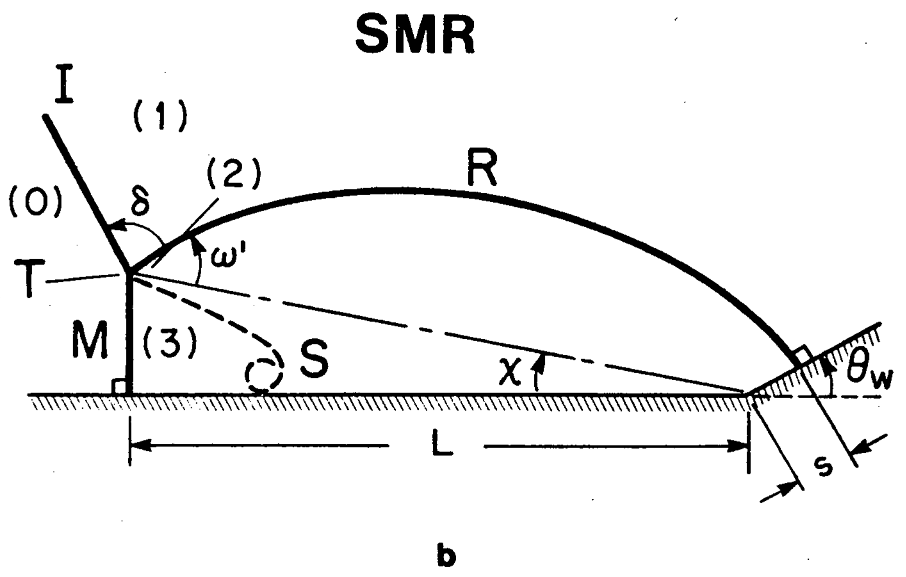

Figure 1b

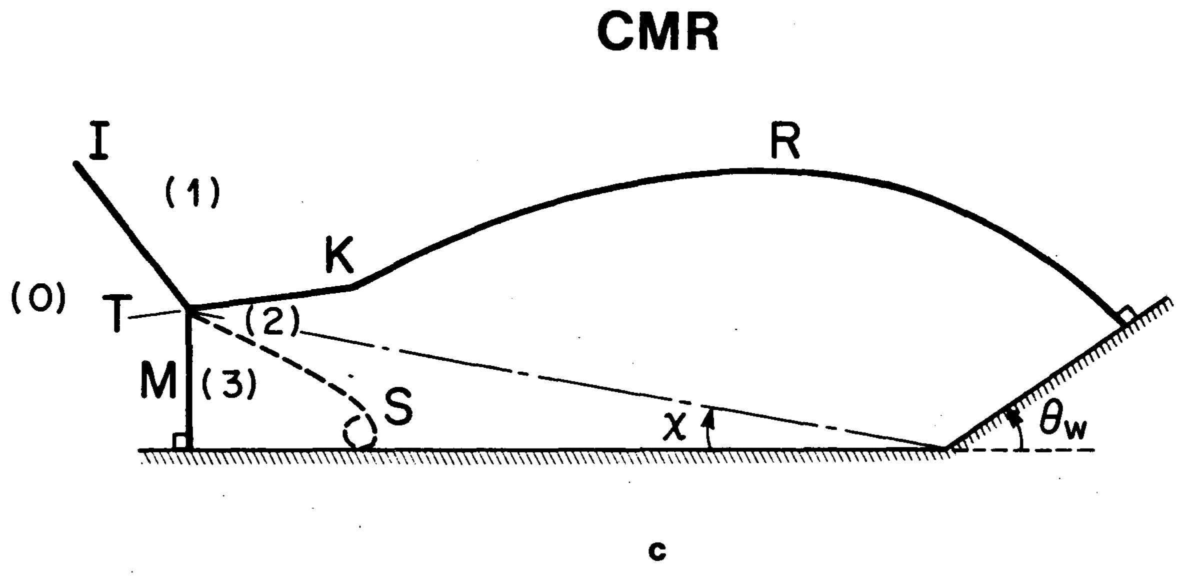

Figure 1c

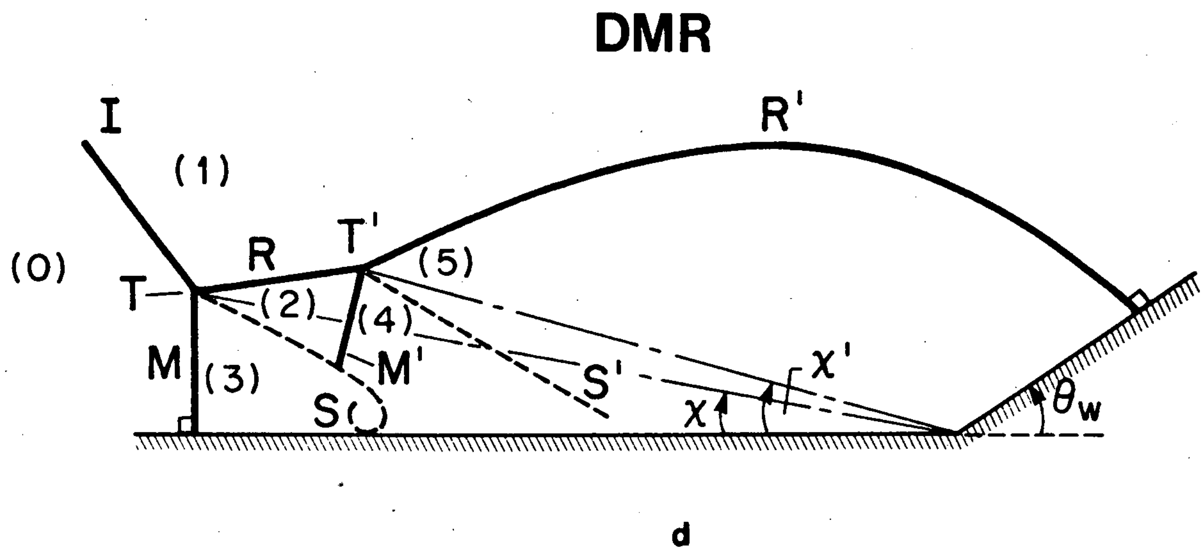

Figure 1d

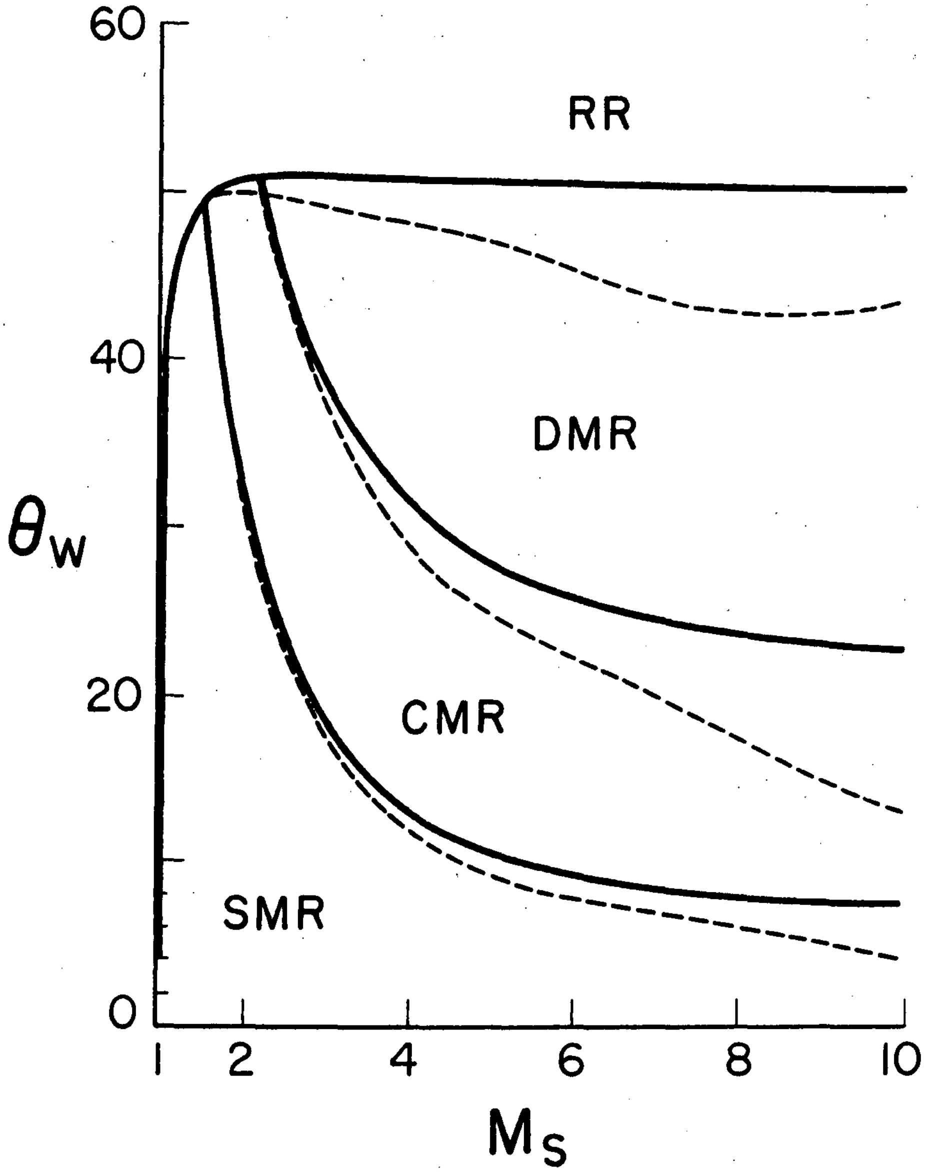

Figure 2

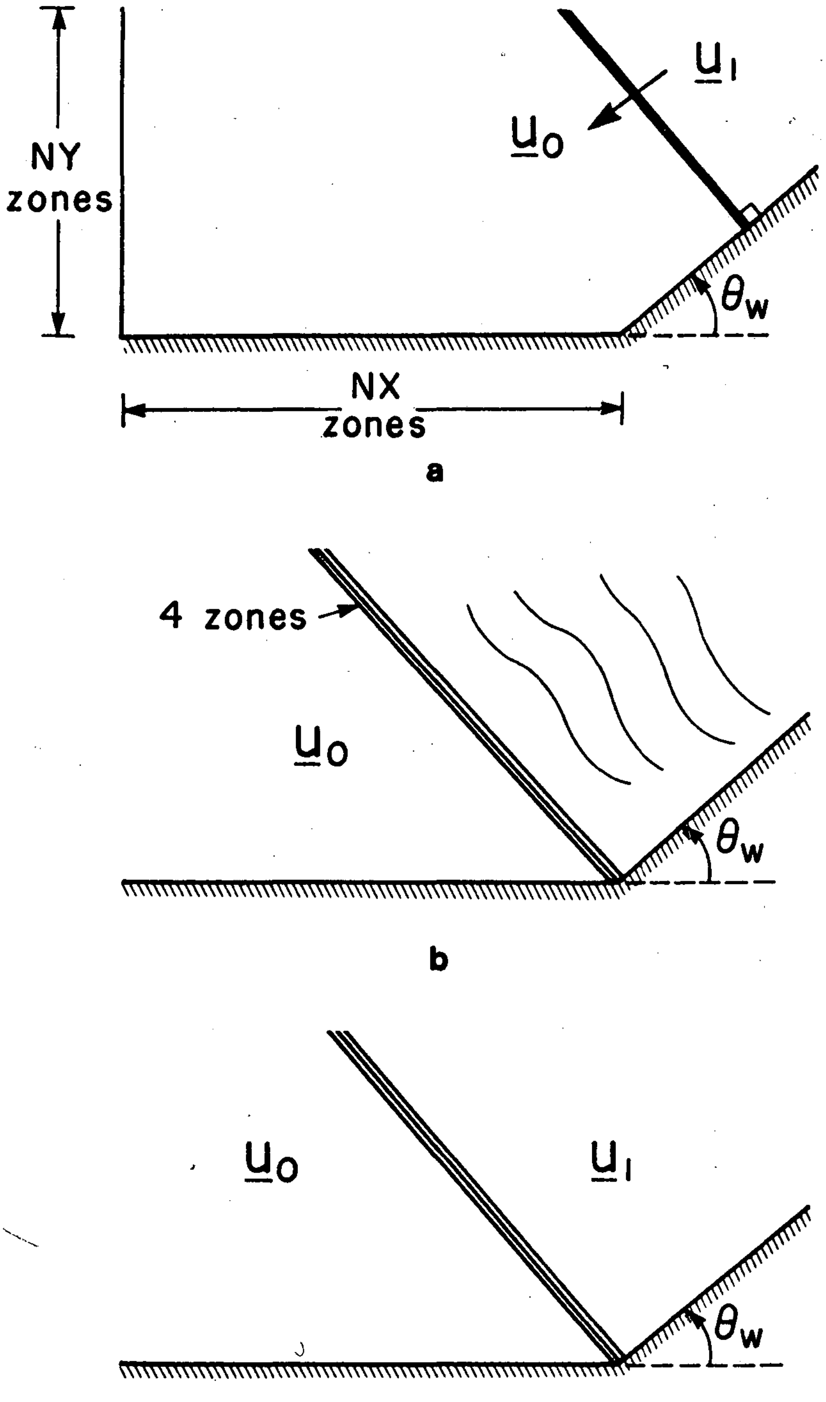

a

b

c

Figure 3a,b,c

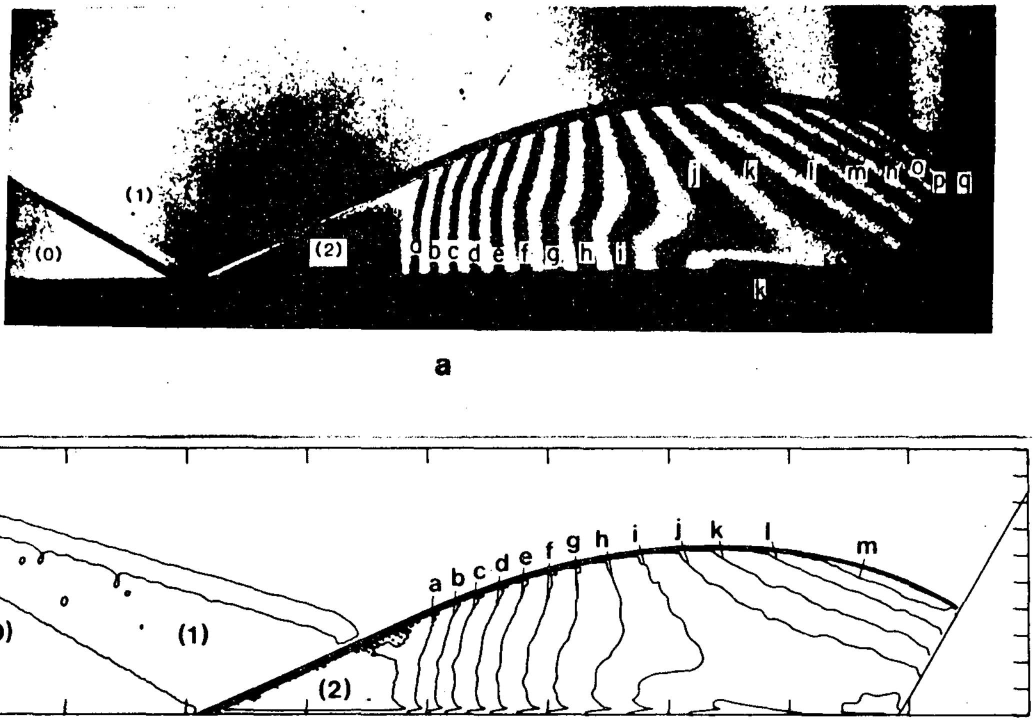

a

b

Region	ρ/ρ_0
(0)	1.00
(1)	2.33
(2)	4.38
a	4.32
b	4.25
c	4.19
d	4.12
e	4.06
f	3.99
g	3.93

Region	ρ/ρ_0
h	3.86
i	3.80
j	3.73
k	3.67
l	3.60
m	3.54
n	3.47
o	3.41
p	3.34
q	3.28

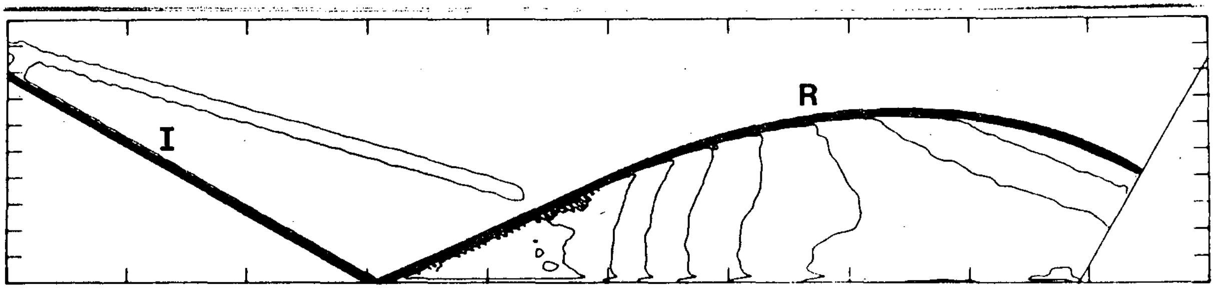

c

Figure 4a,b,c

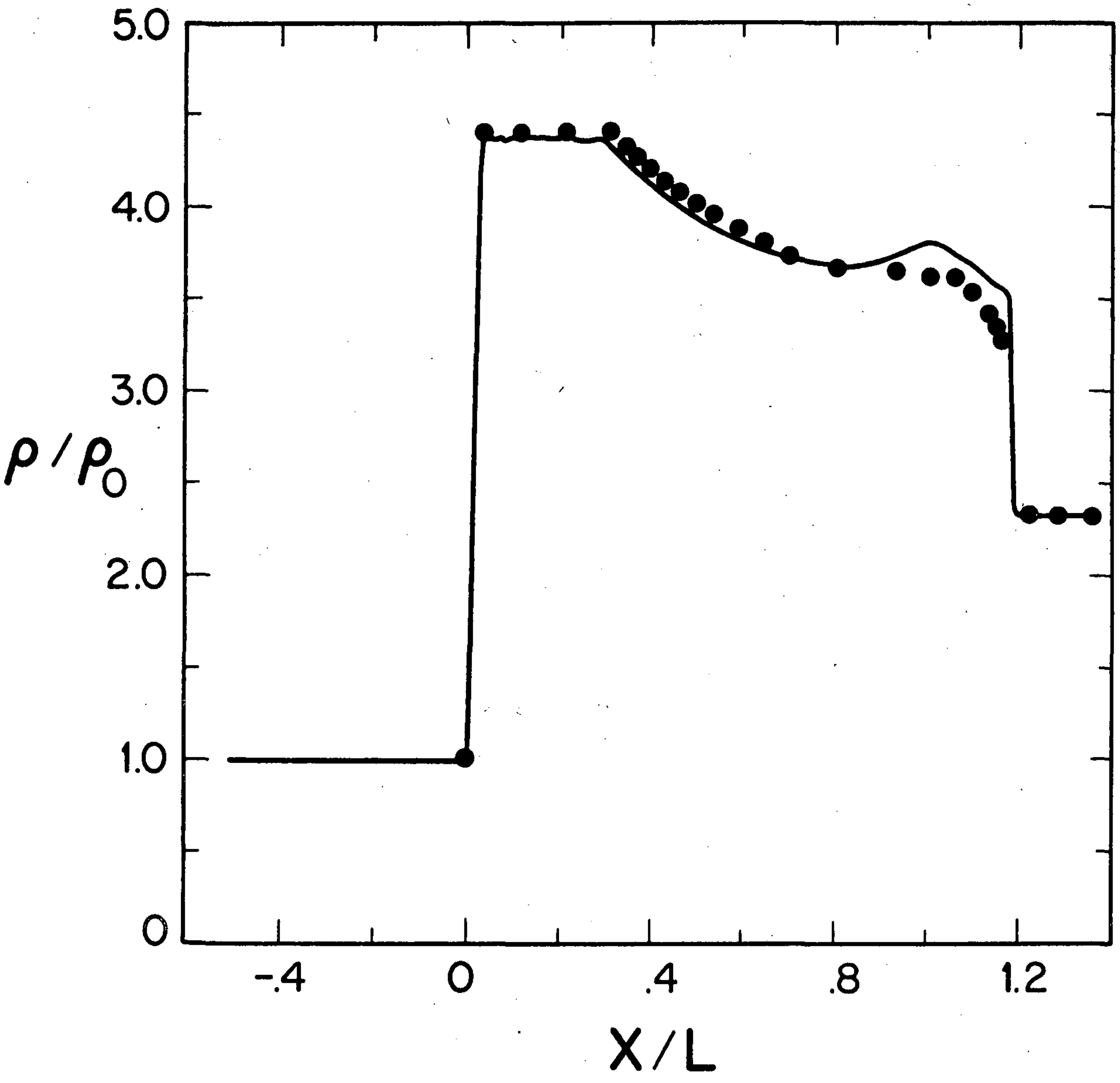

d

Figure 4d

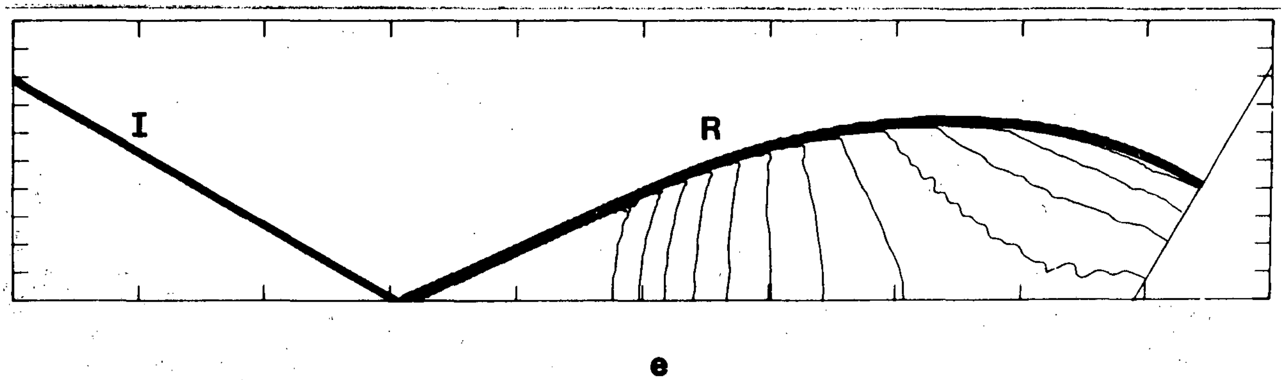

Figure 4e

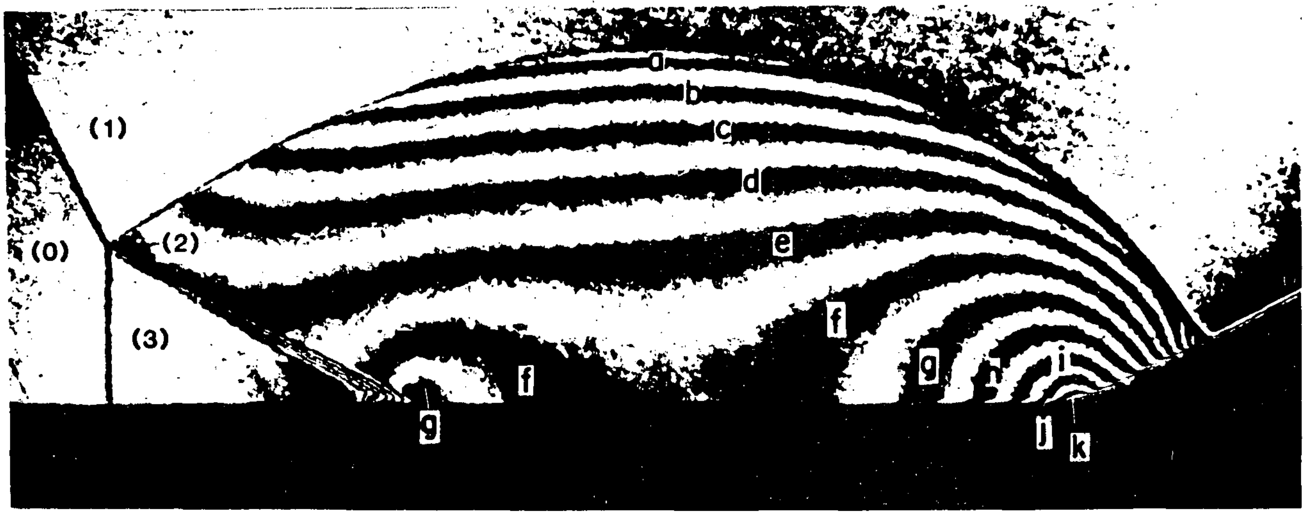

a

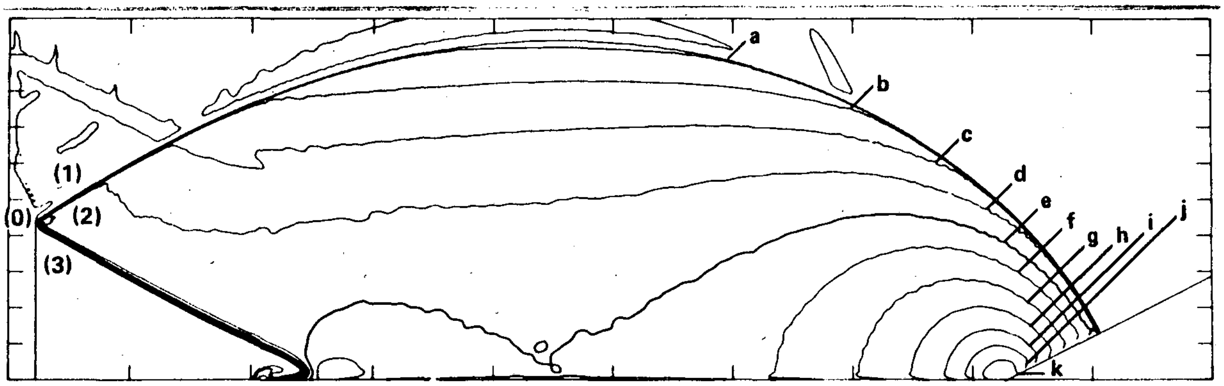

b

REGION	ρ/ρ_o
0	1.00
1	2.71
2	3.68
3	3.33
a	3.36
b	3.44
c	3.52
d	3.60

REGION	ρ/ρ_o
e	3.68
f	3.75
g	3.83
h	3.91
i	3.99
j	4.06
k	4.14

Figure 5a,b

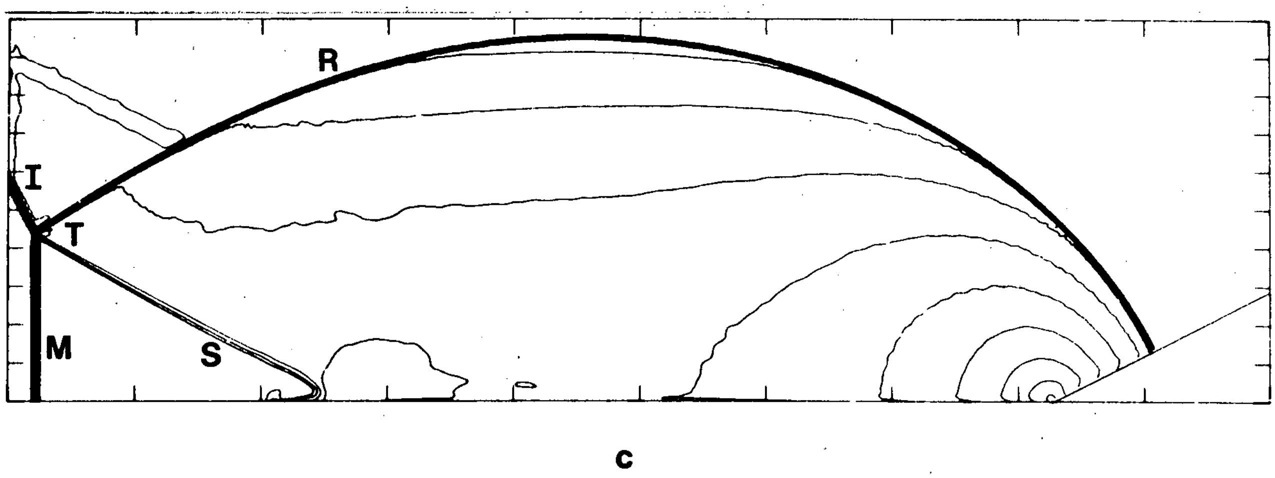

Figure 5c

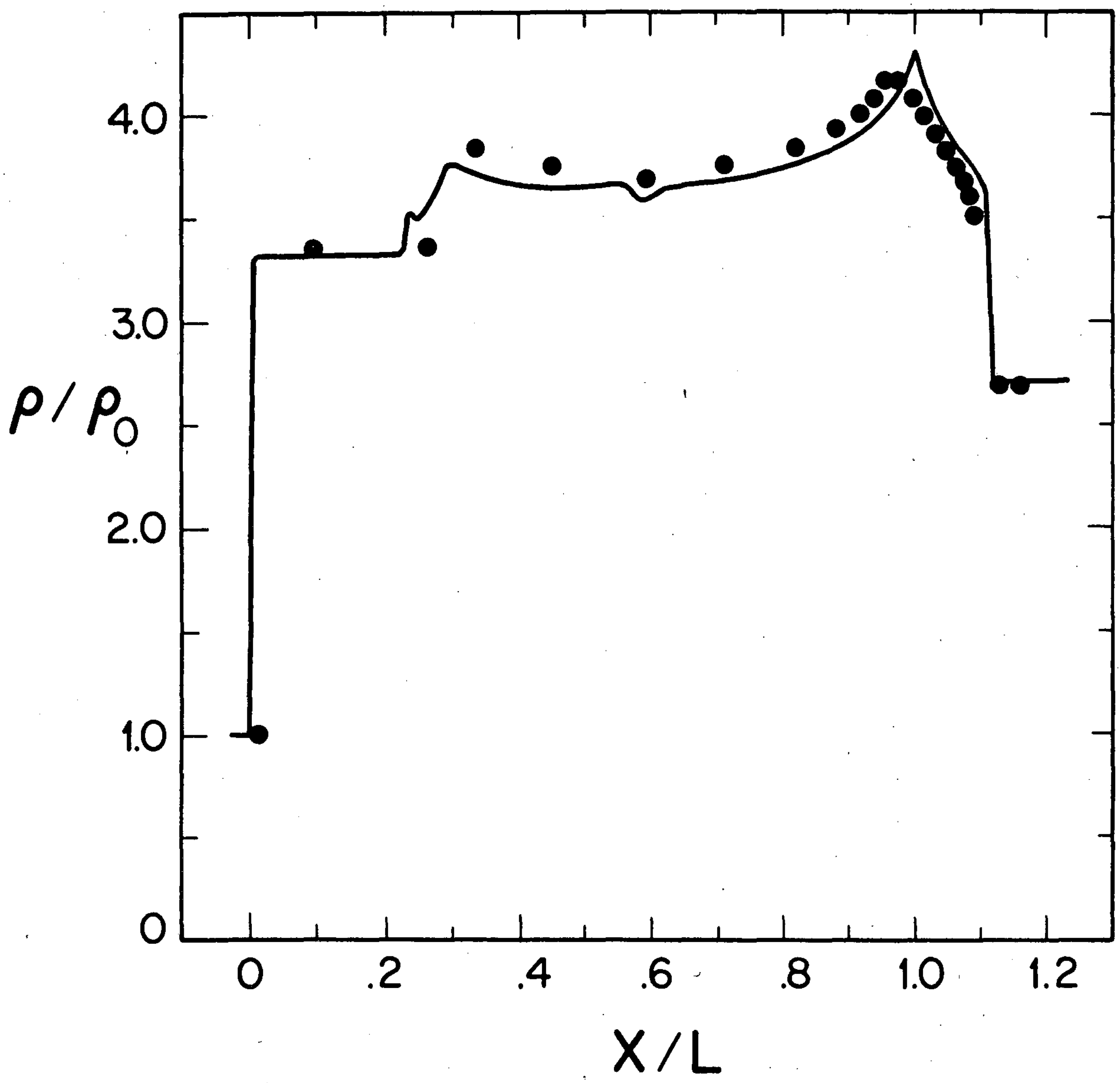

d

Figure 5d

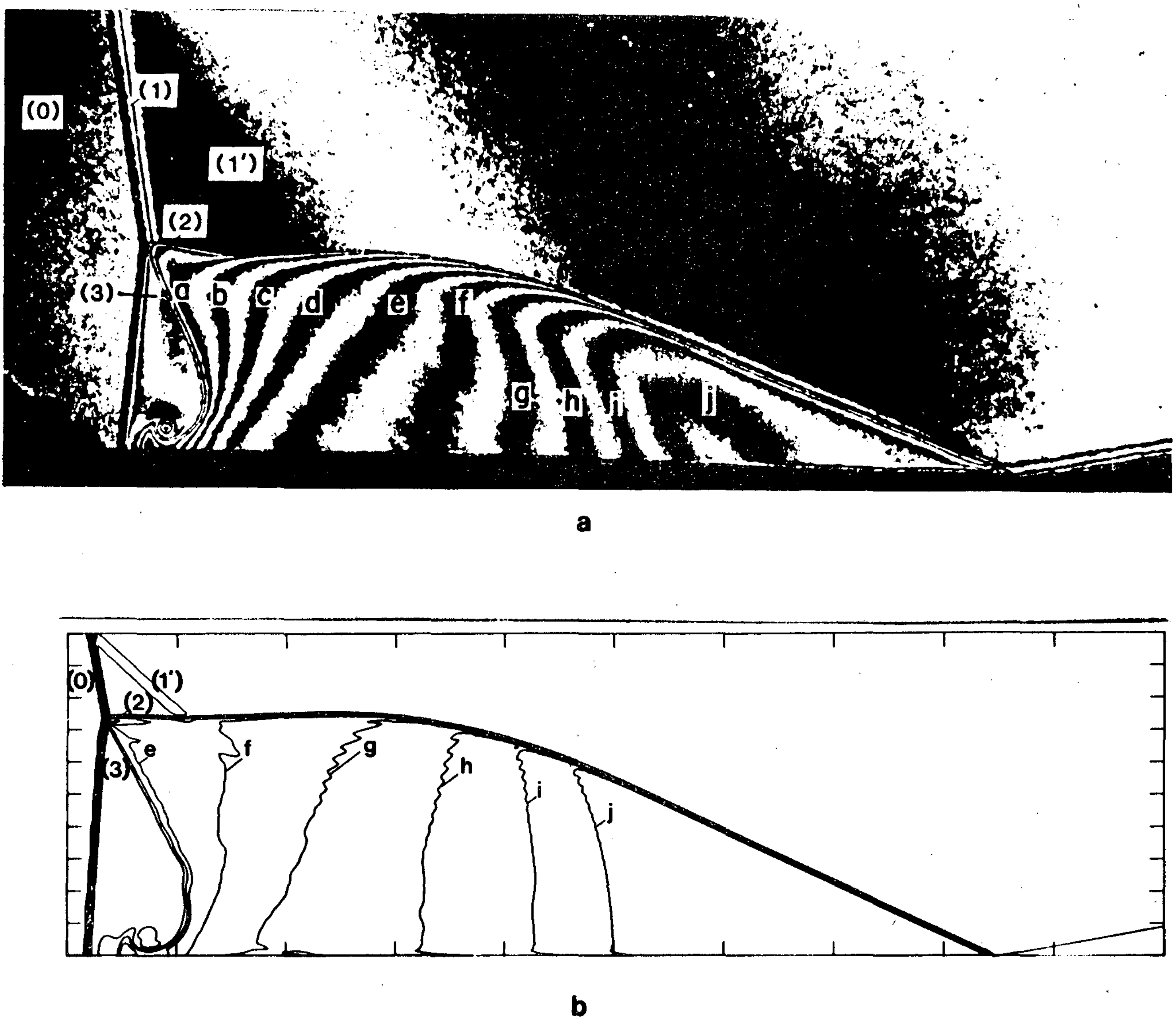

Region	ρ/ρ_0
(0)	1.00
(1)	5.73
(1')	6.33
(2)	6.30
(3)	5.77
a	6.70
b	7.10
c	7.50
d	7.90
e	8.29
f	8.69
g	9.09
h	9.49
i	9.89
j	10.29

Figure 6a,b

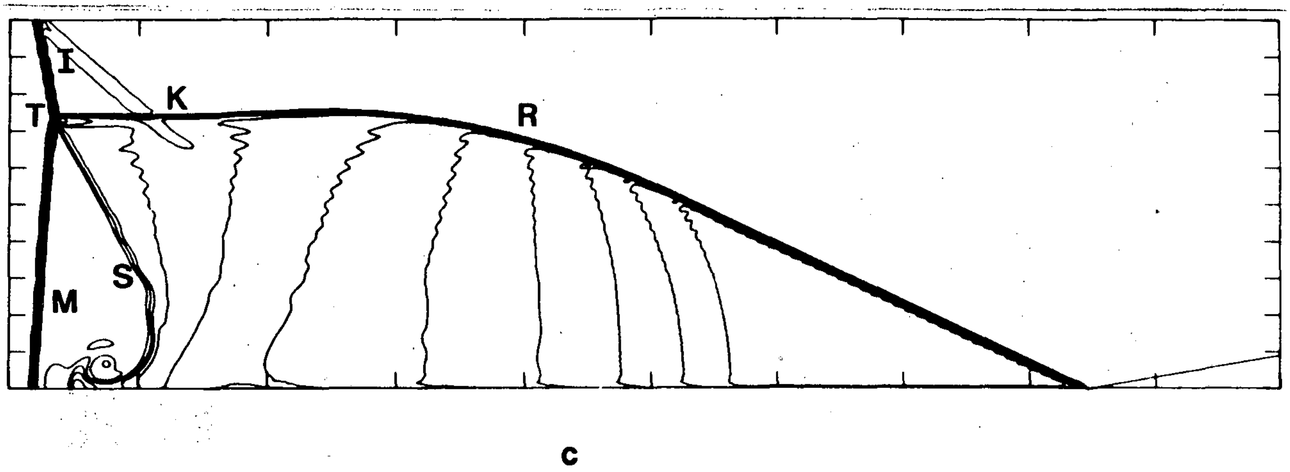

Figure 6c

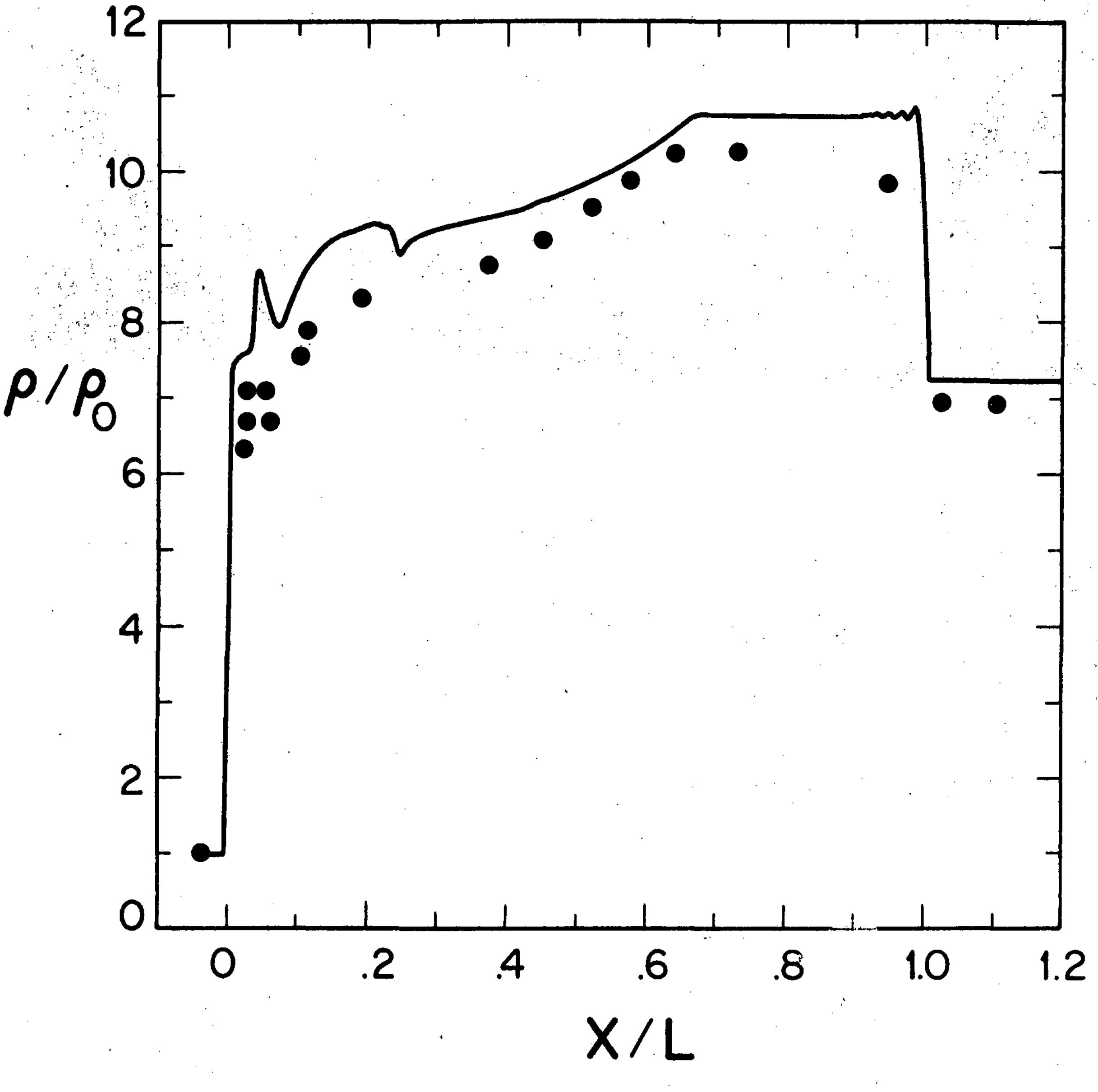

d

Figure 6d

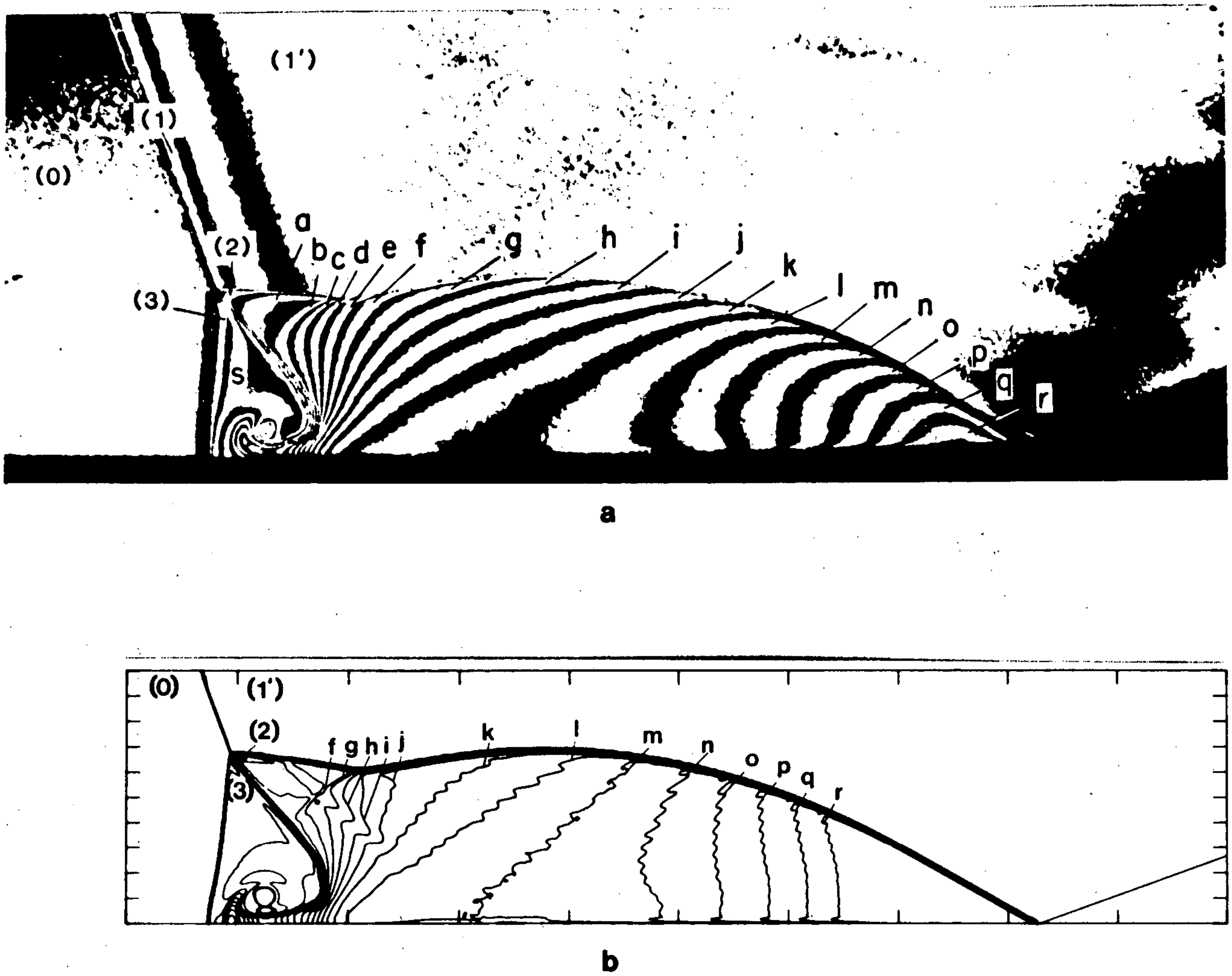

Region	ρ/ρ_0
(0)	1.00
(1)	5.47
(1')	6.13
(2)	6.65
(3)	5.59
a	6.97
b	7.30
c	7.62
d	7.94
e	8.27
f	8.59
g	8.91
h	9.24
i	9.56
j	9.88
k	10.21
l	10.53
m	10.85
n	11.18
o	11.50
p	11.82
q	12.15
r	12.47
s	5.91

Figure 7a.b

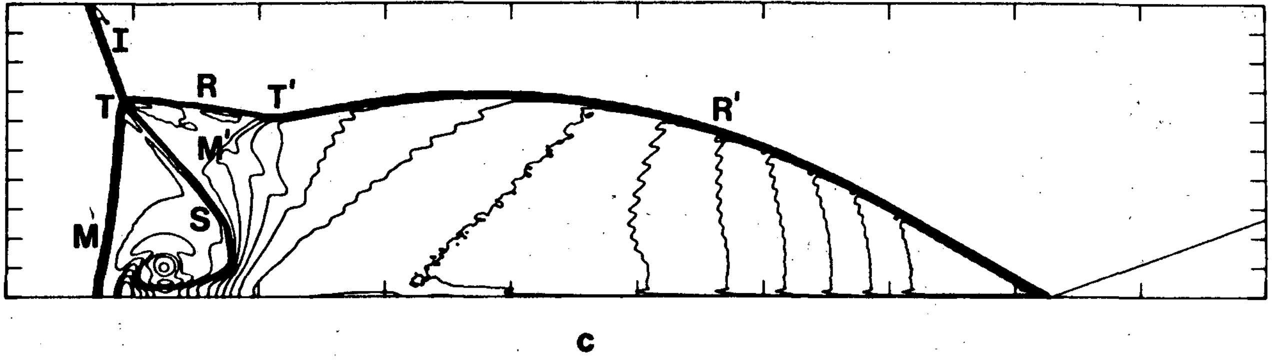

Figure 7c

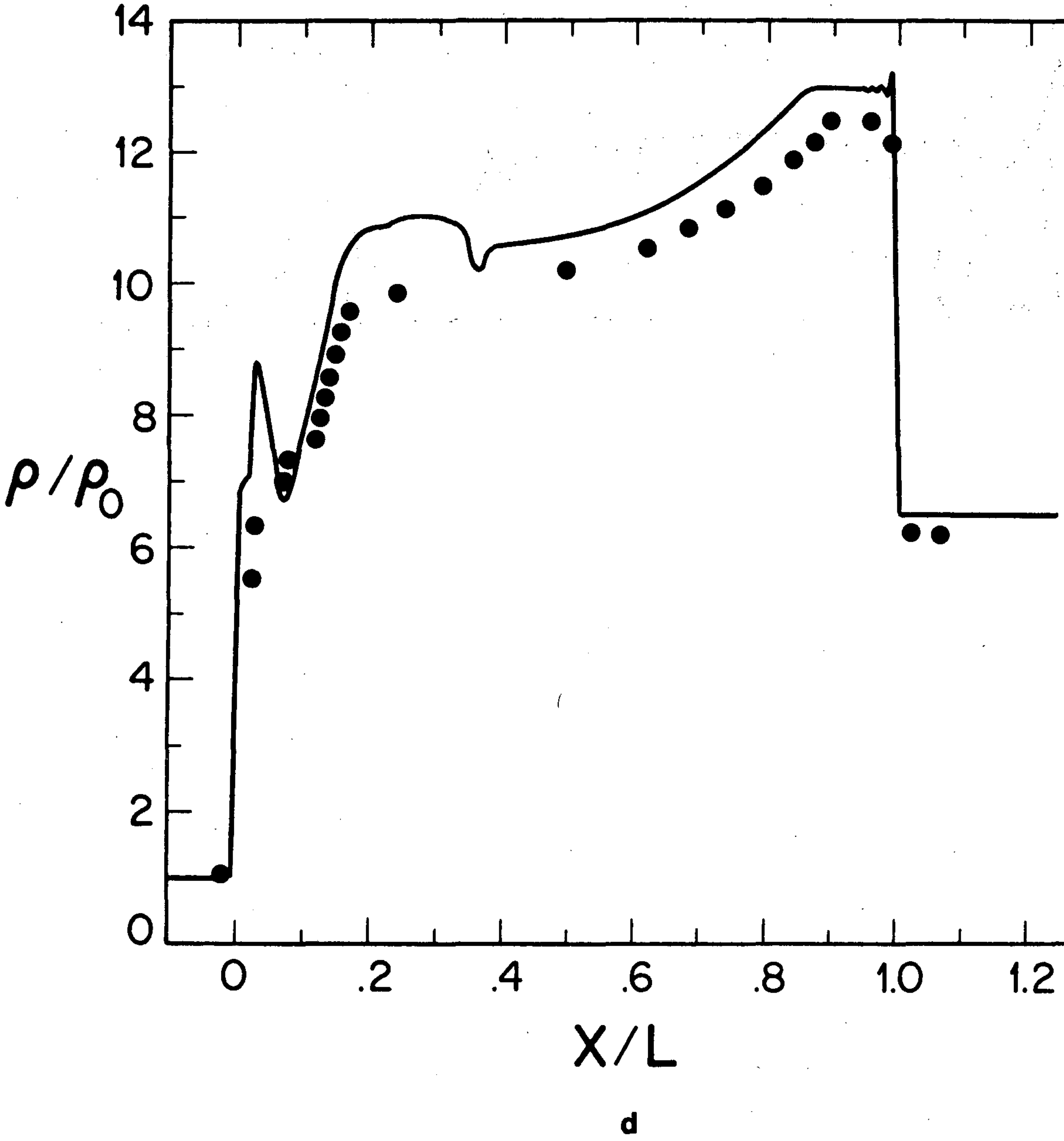

Figure 7d

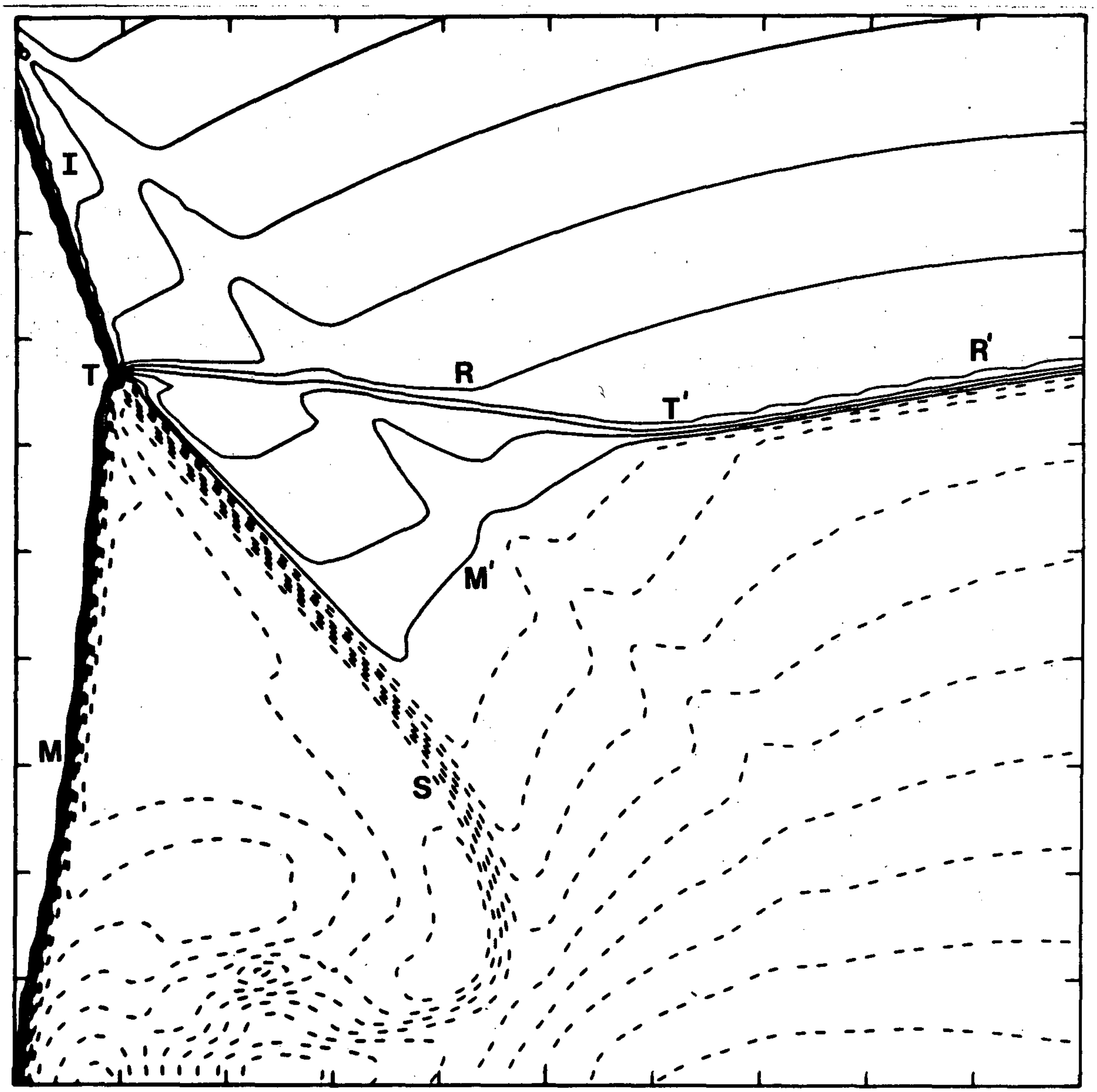

e

Figure 7e

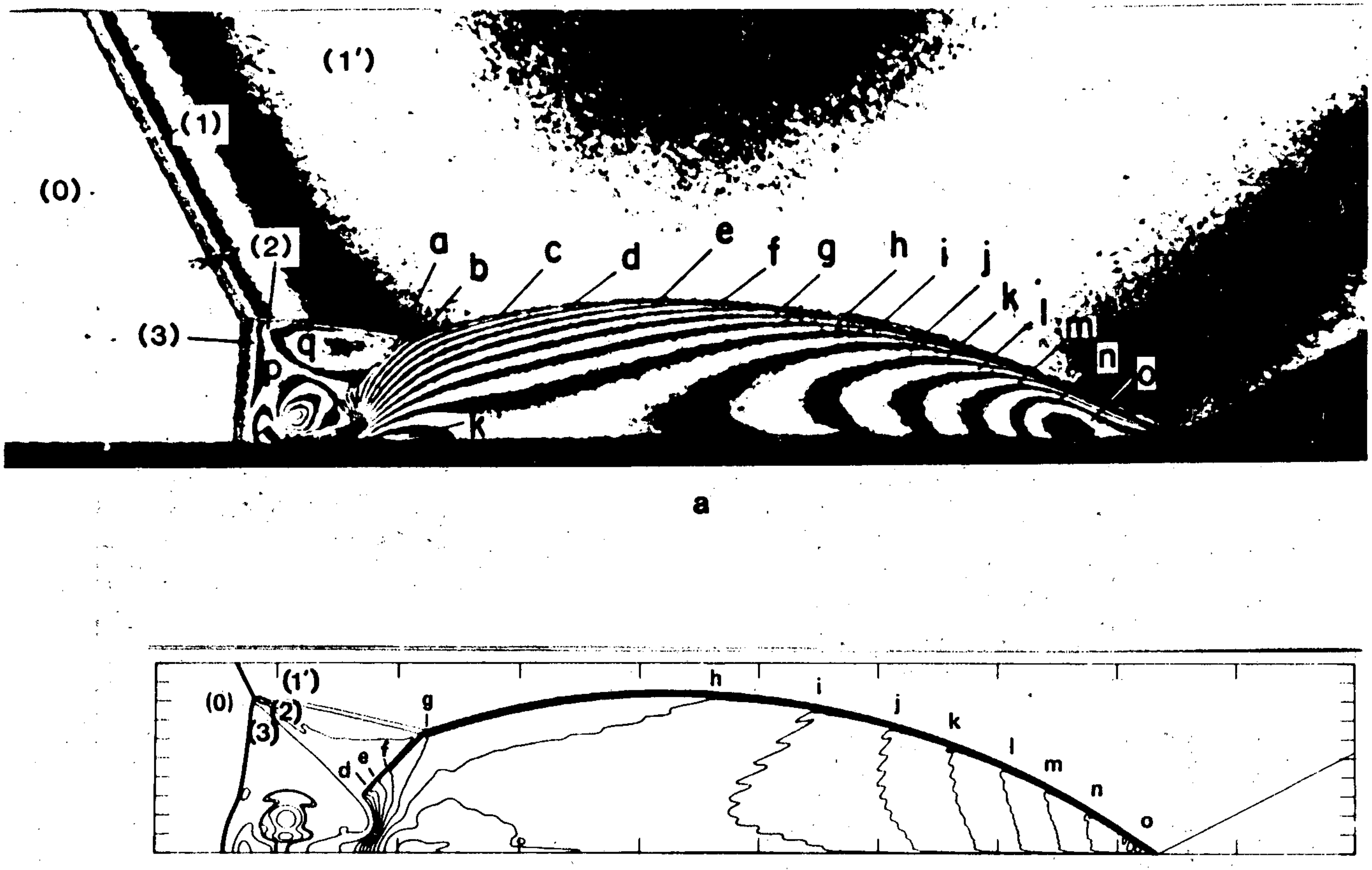

a

b

REGION	ρ/ρ_0
(0)	1.00
(1)	5.63
(1′)	6.89
(2)	7.44
(3)	5.74
a	9.53
b	10.16
c	10.79
d	11.42
e	12.05
f	12.68

REGION	ρ/ρ_0
g	13.32
h	13.95
i	14.58
j	15.21
k	15.84
l	16.47
m	17.10
n	17.73
o	18.36
p	6.37
q	8.07

Figure 8a,b

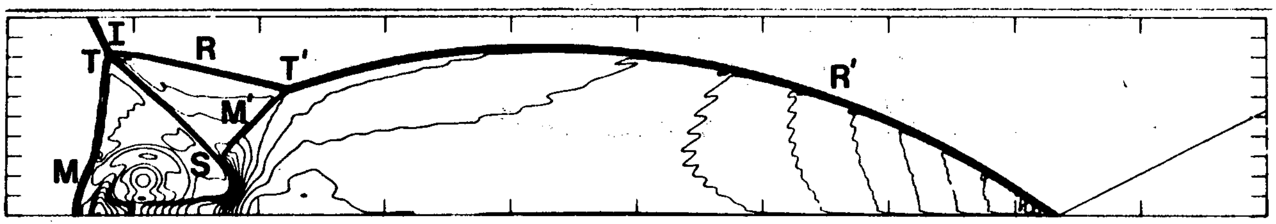

c

Figure 8c

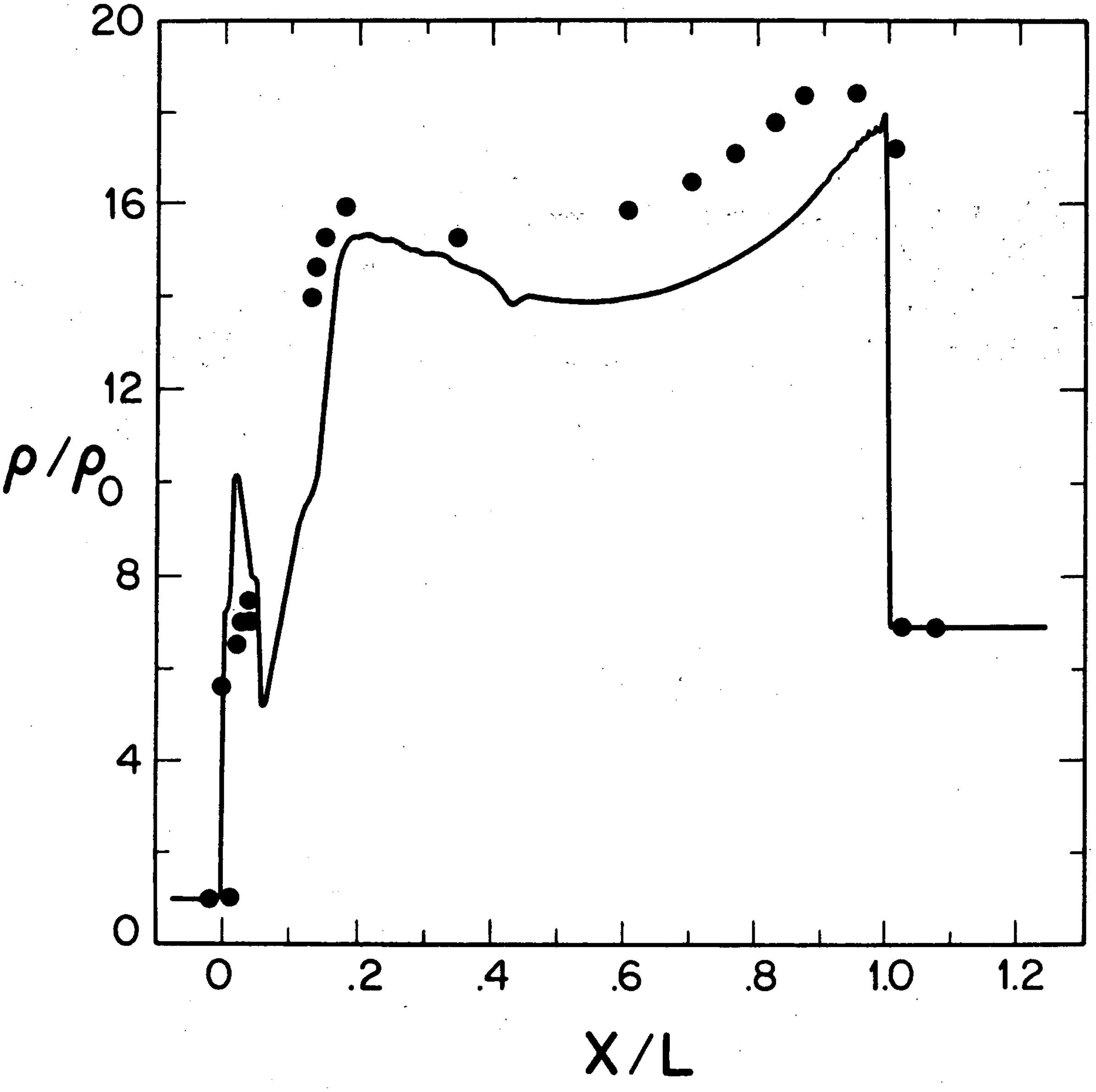

d

Figure 8d

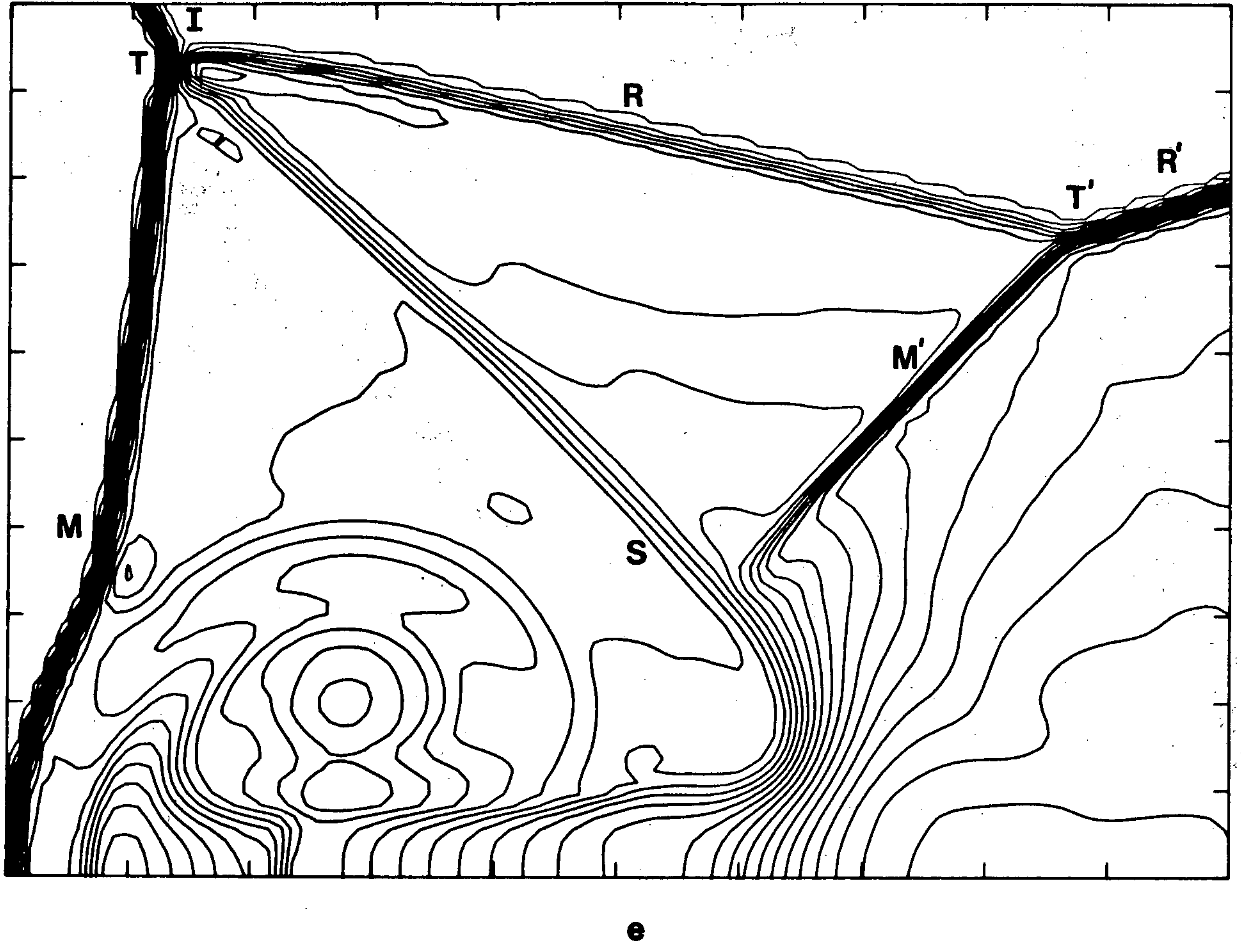

Figure 8e

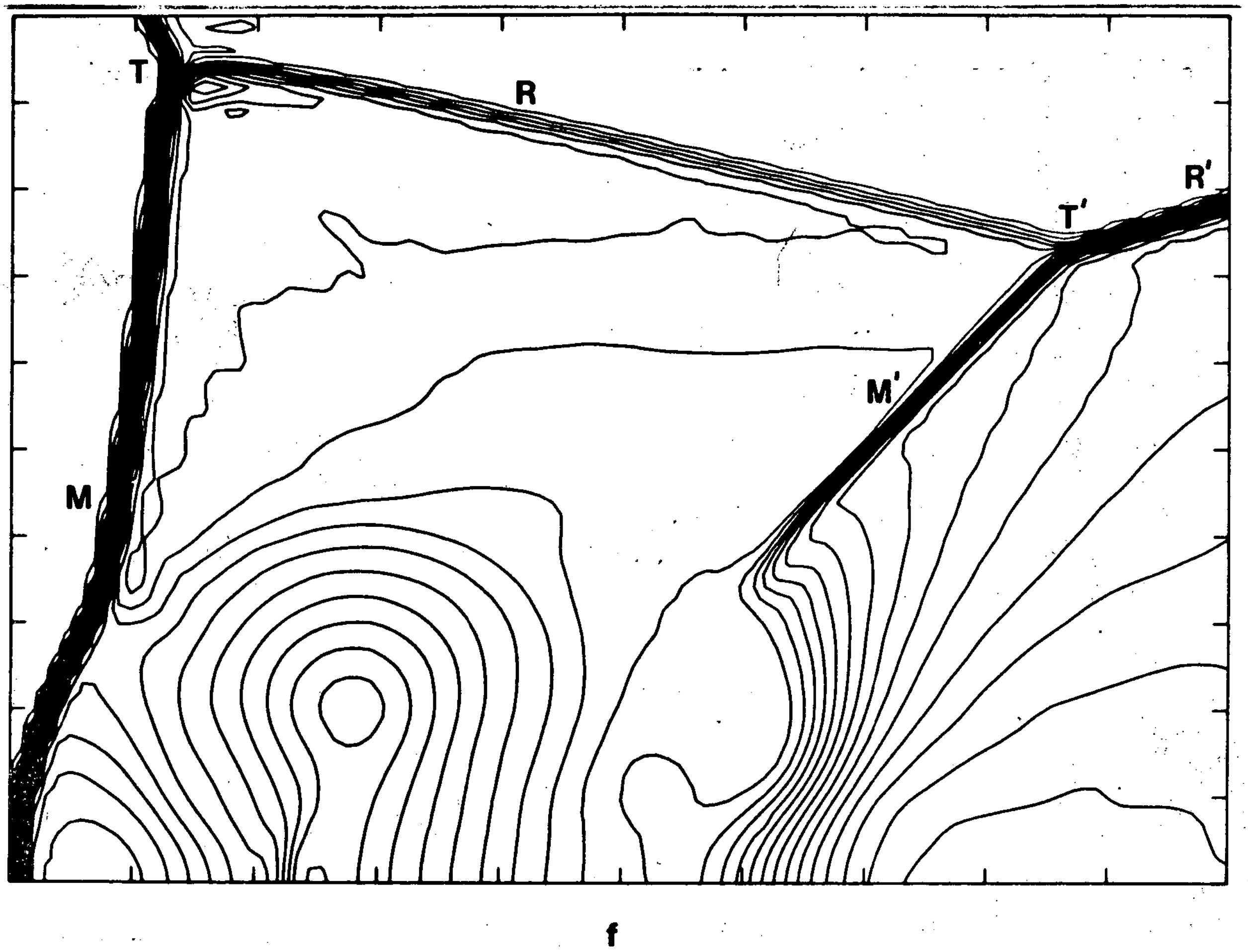

Figure 8f

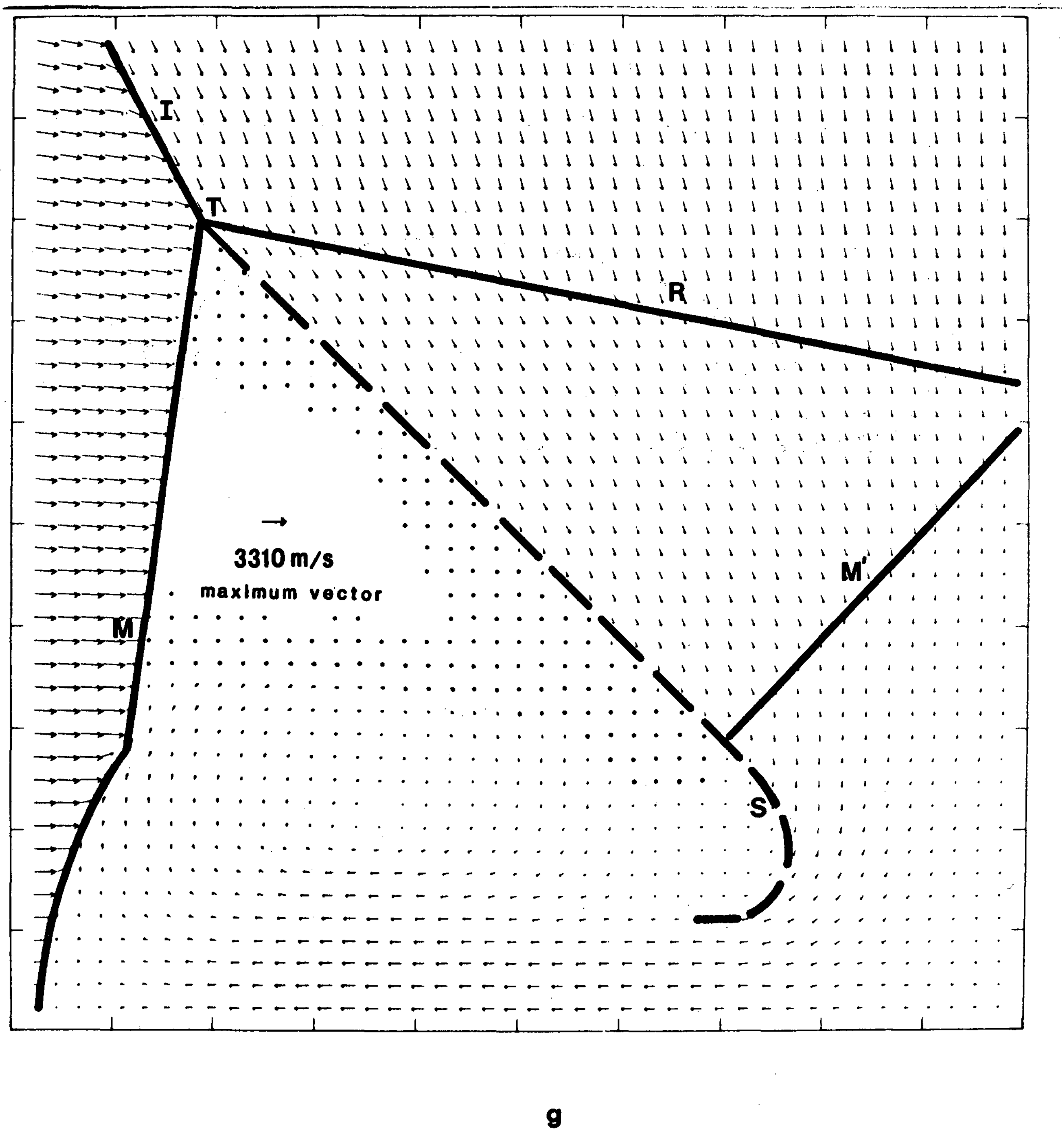

Figure 8g

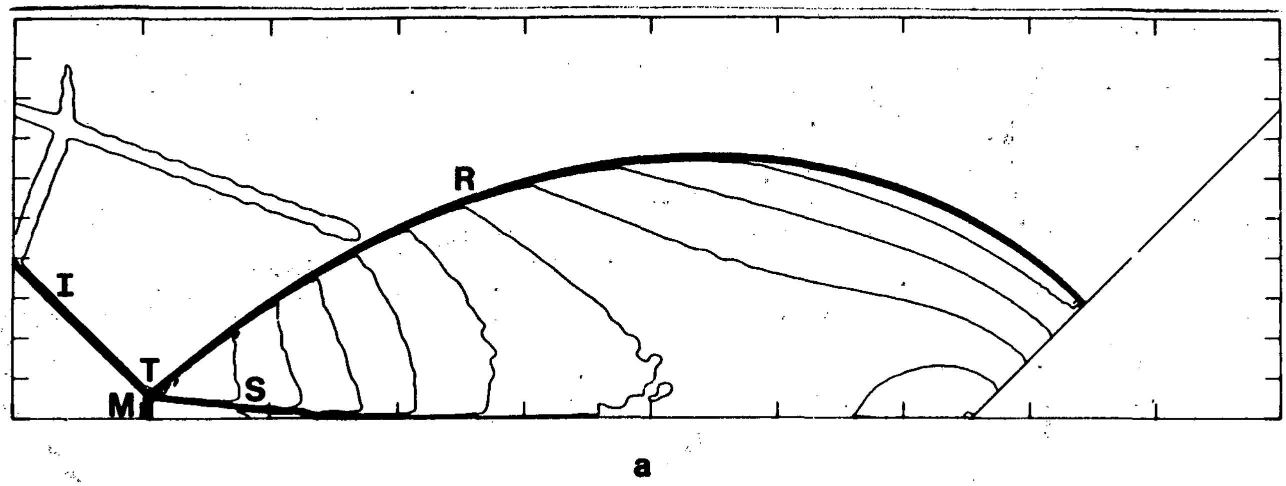

Figure 9a

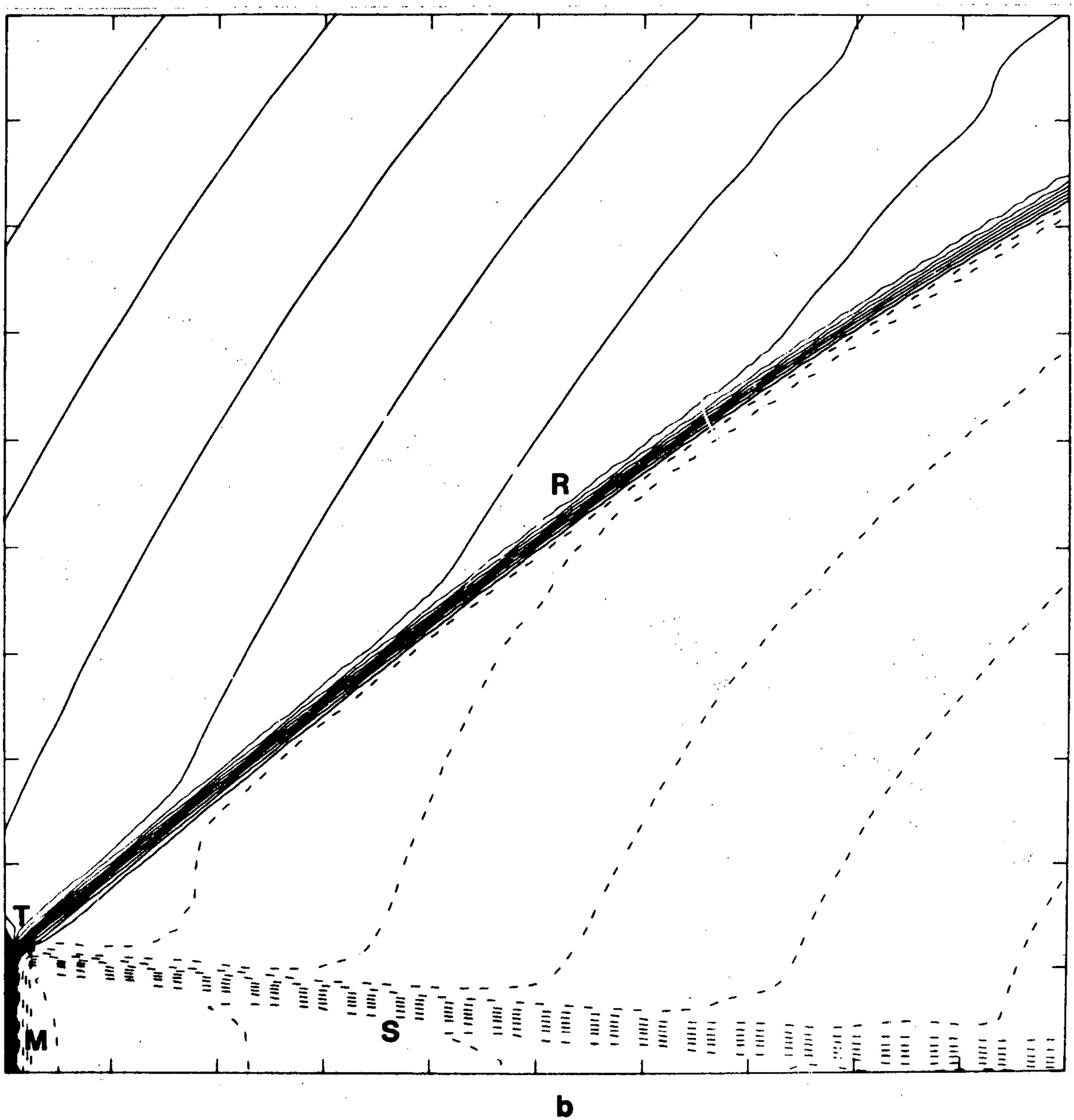

Figure 9b

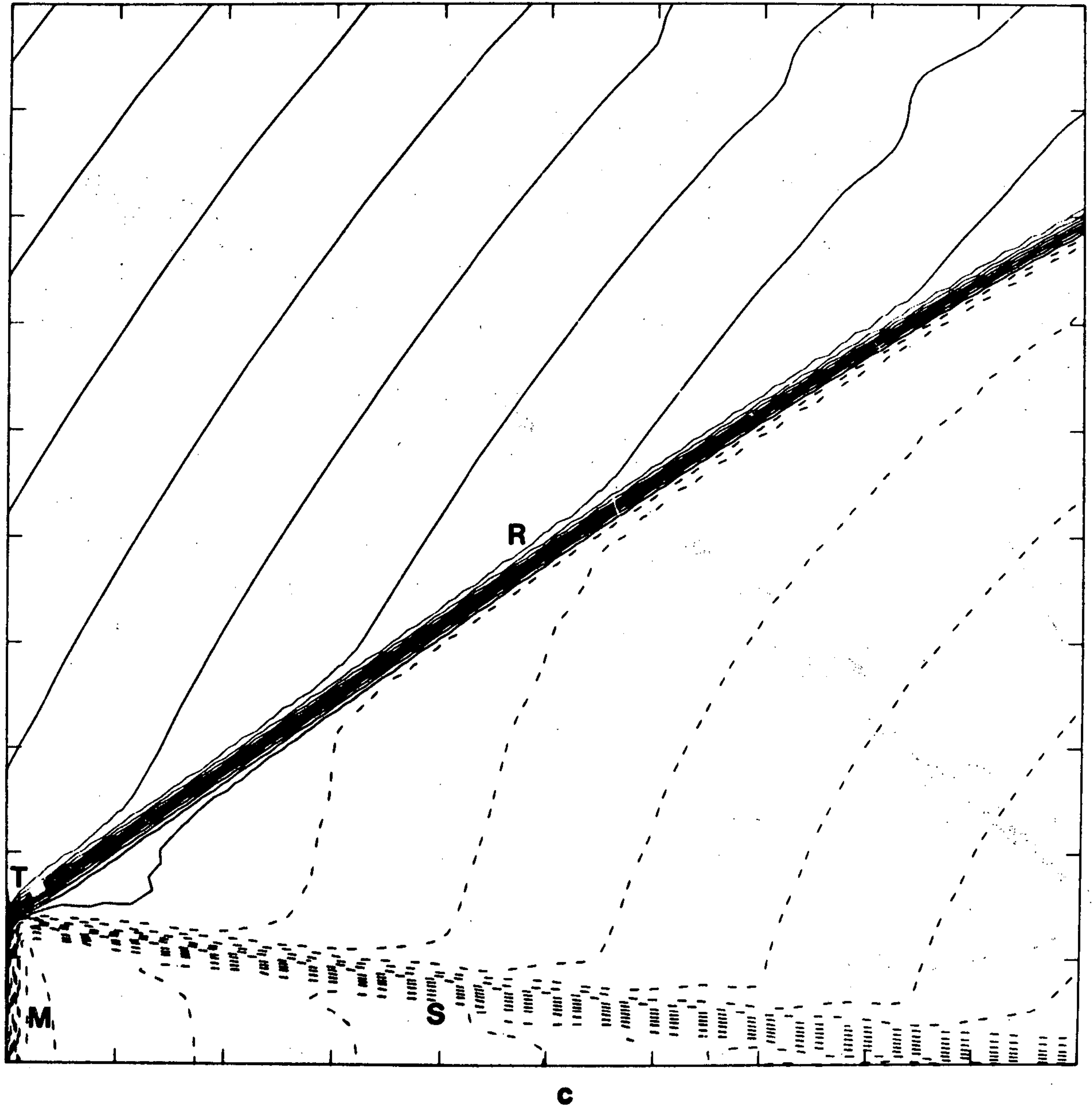

Figure 9c

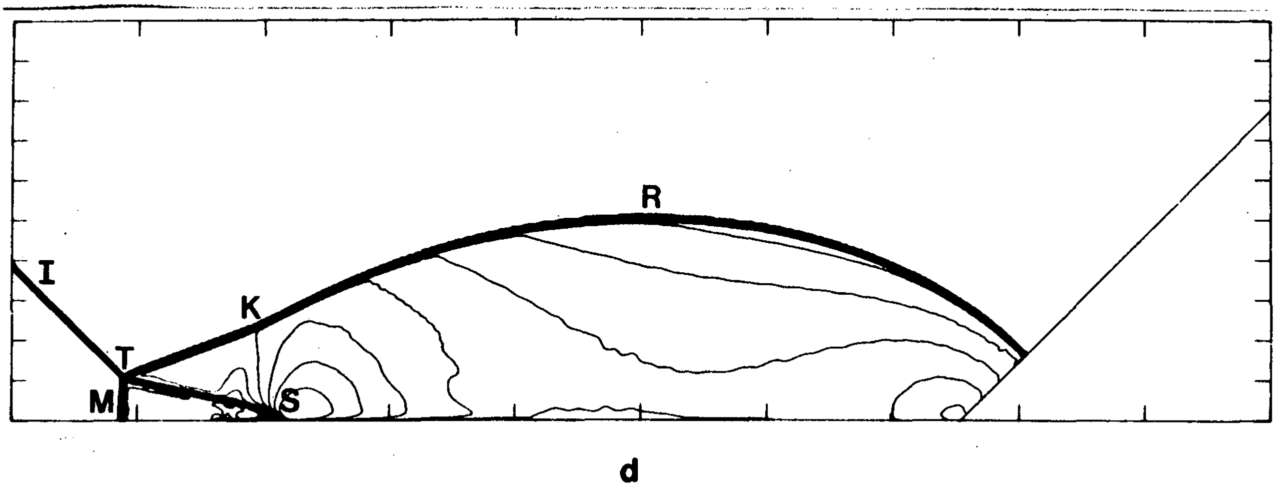

Figure 9d

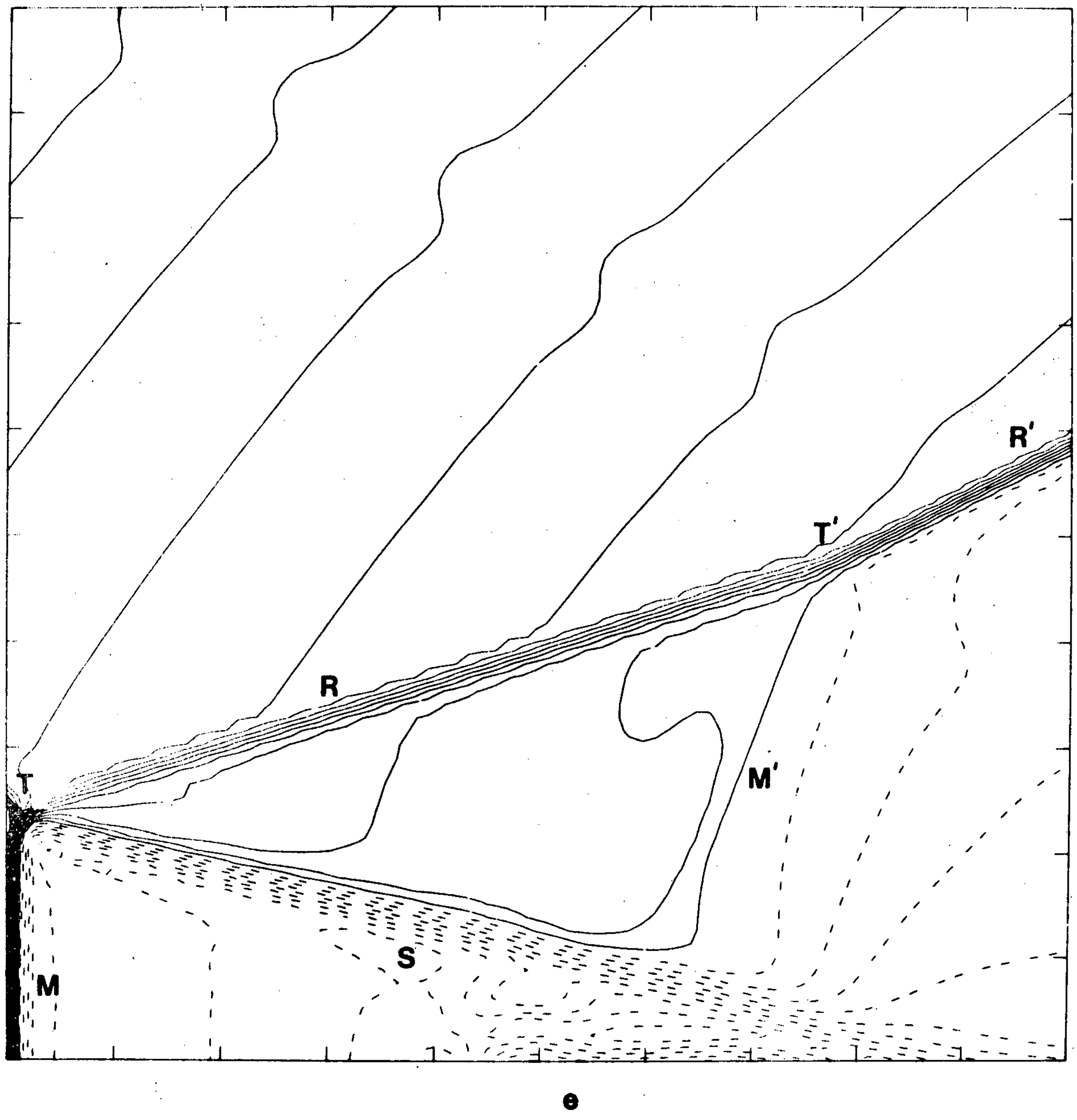

Figure 9e

a

Region	ρ/ρ_0
(0)	1.00
(1)	3.78
(2)	6.69
(3)	3.91
a	7.94
b	9.19
c	6.69
d	5.44

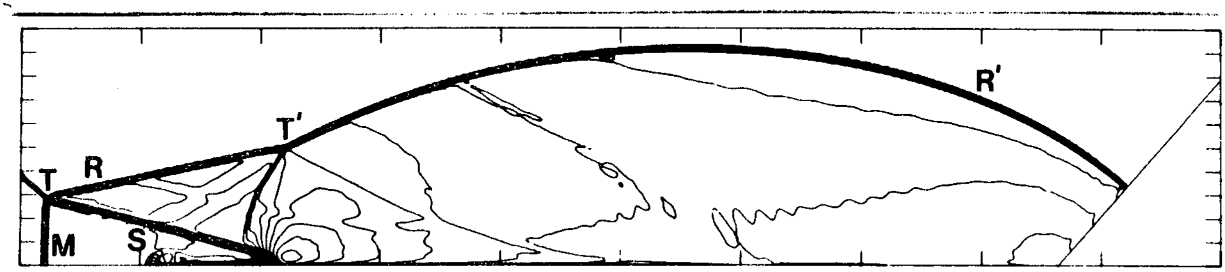

b

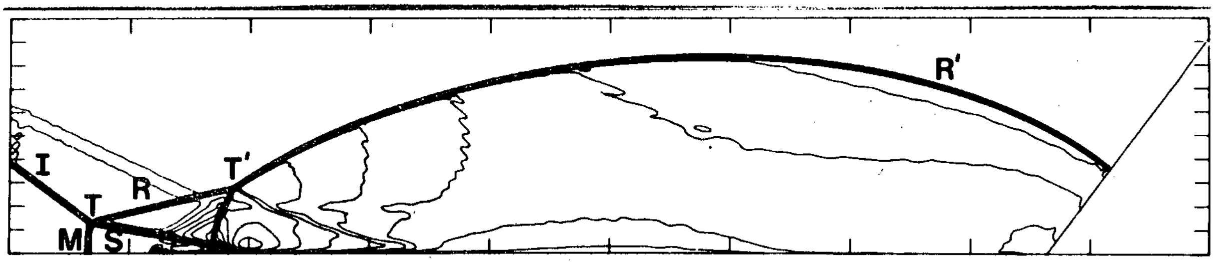

c

Figure 10a,b,c

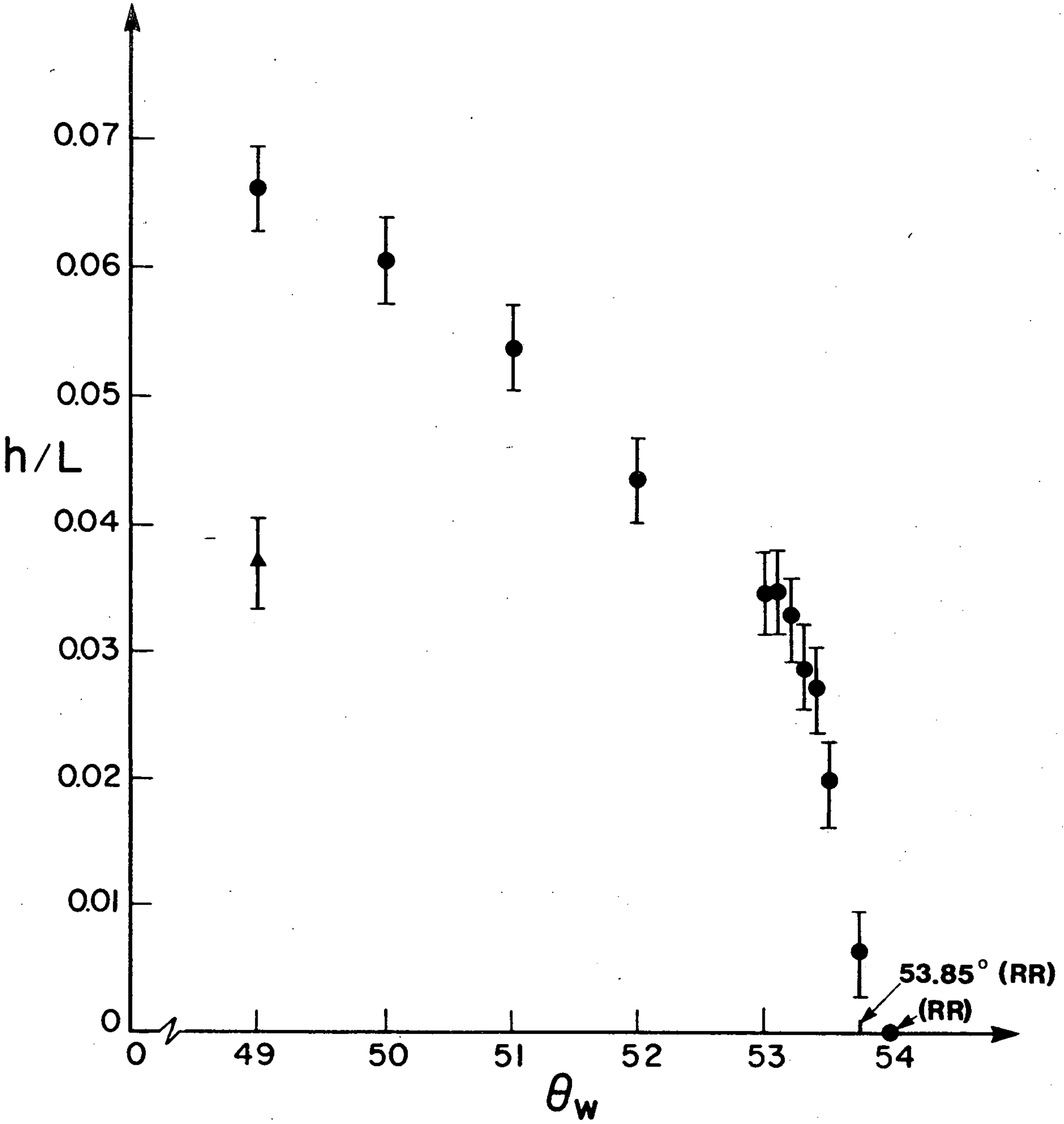
h/L
0.07
0.06
0.05
0.04
0.03
0.02
0.01
0
0
49
50
51
52
53
54
θ_w
53.85° (RR)
(RR)

d

Figure 10d

TECHNICAL INFORMATION DEPARTMENT
LAWRENCE BERKELEY LABORATORY
UNIVERSITY OF CALIFORNIA
BERKELEY, CALIFORNIA 94720